Appendix 4
Pielikums 4

National Research Programme

„Cyber-physical systems, ontologies and biophotonics for safe&smart city and society"

(SOPHIS)

Project No.4

Development of technologies for secure and reliable smart city"

(GudPils)

Period 3

2016

Contents

Appendix 4.5: Remote Life-sign Detection: movement, breathing, hearbeat
Appendix 4.6: Long term drinking water quality monitoring in drinking water supply systems by on-line sensors
Appendix 4.7: Behavior and stability of adenosine triphosphate (ATP) during chlorine disinfection
Appendix 4.8: A pipeline for developing and testing staining protocols for flow cytometry

Glossary and abbreviations

ANN - artificial neural network;

API - application program interface;

ASDM - Asynchronous Sigma-Delta modulator;

ATP - adenosine triphosphate;

AWG - arbitrary waveform signal generator;

B2B - band to band;

BER - bit error rate;

CNN - convolution neural network;

CUDA - NVIDIA parallel computing platform on GPU;

DFB - distributed feedback laser;

DL - deep learning;

DMSO - dimethyl sulfoxide;

DSF - dispersion shifted fiber;

DSO - digital storage oscilloscope;

DSP - digital signal processing;

DWDS - drinking water distribution system;

DWSS – drinking water supply system;

EC – electrical conductivity;

EDI - Institute of Electronics and Computer Science, Riga, Latvia;

EDS - event detection system;

EDTA - ethylenediaminetetraacetic acid;

EPA - United States Environmental Protection Agency;

ERDF - European Regional Development Fund;

ETSI - European Telecommunications Standards Institute;

FCM - flow cytometry;

FFT - fast Fourier transform;

FMCW - frequency-modulated continuous-wave;

GbE - Gigabit Ethernet;

GPR - ground probing radar;

GPS - Global Positioning System;

GPU - graphics processing unit;

GudPils - Development of technologies for secure and reliable smart city (Project No. 4);

GUI - graphical user interface;

HPC - High Performance Computing;

HtPC – heterotrophic plate count;

IC – inorganic carbon;

ICC - intact cell count;

IFFT - inverse fast Fourier transform;

KL - Karhunen-Loeve;

OS - computer Operating System;

LabVIEW - Laboratory Virtual Instrument Engineering Workbench (National Instruments software environment);

LCD - Liquid Crystal Display;

LSTM - Long Short-Term Memory network;

NDVI - Normalized Difference Vegetation Index;

NPOC – non-purgeable organic carbon;

NRZ - non-return-to-zero;

NVIDIA - NVIDIA Corporation;

NZDSF - non-zero dispersion-shifted fiber;

OF - optical fiber;

ORP – oxidation-reduction potential;

OS - computer Operating System;

PC - personal computer;

PCB - printed circuit board;

RGB - red-green-blue;

PI – propidium iodide;

RMS - root mean square;

RNN - recurrent neural network;

RTU - Riga Technical University;

RTU TI - Riga Technical University Telecommunications Institute;

RTU WRL - Riga Technical University Faculty of Civil Engineering Water Research Laboratory;

RTU BF - Riga Technical University Faculty of Civil Engineering;

SG – SYBR Green I;

SGPI – SYBR Green I propidium iodide stain;

SNR - Signal-to-noise ratio;

SMF - single-mode optical fiber;

SOPHIS - programme "Cyber-physical systems, ontologies, and bio-photonics for safe&smart city and society";

SRD - Short Range Devices;

SVM - Support Vector Machine;

TCC - total cell count;

TDM-PON - time division multiplexed passive optical network;

TI image - thermal infrared image;

TC – total carbon;

TOC - total organic carbon;

TWI - Through-Wall Imaging;

USB - Universal Serial Bus;

UWB - Ultra-wideband;

VPP - State Research Programme;

VOA - variable optic attenuator;

WDM-PON - wavelength division multiplexed passive optical network;

WTP – drinking water treatment plant;

Chapter 4.1

Introduction

This appendix contains the scientific report of the project GudPils for the third period of the SOPHIS programme.

The overall objective of the project and its tasks were described in previous reports and will not be repeated here. The tasks defined by the scientific groups for the third period are listed in the summary report of the programme. Here we present a detailed description of the research work and results obtained during the third period of the programme. Results described in scientific publications are not repeated; publications are attached as annexes of this report instead and referenced in the text.

The report consists of sections prepared by each scientific group. These are as follows:

1. EDI BIGDATA group develops methods and software for video and other sensor data processing to target urban security problems. The results of this group is presented in chapter 4.2;

2. EDI REMSENS group develops remote sensing data processing techniques for monitoring of the urban environment. The results of this group is presented in chapter 4.3;

3. EDI RADAR group develops ultra-wideband radar technology-based solutions for urban security systems' needs. The results of this group is presented in chapter 4.4;

4. RTU TI group of researchers develops optical networking solutions for smart cities data transmission. The results of this group is presented in chapter 4.5;

5. RTU WRL team (previously referred as RTU BF) of researchers develops solutions for controlling the urban water supply systems. The results of this group is presented in chapter 4.6.

Chapter 4.2

EDI BIGDATA group: Development of methods and software for video and other sensor data processing to target urban security problems

The following tasks were focused on during the period 3:

1. Development of a technique for obtaining image descriptors and use it within an example of face recognition;
2. Development of the method for generation of training data for RNN- based object detector.

4.2.1 Development of a technique for obtaining image descriptors and an its application example for face recognition

The progress achieved during the reporting period in development of the technique for using image descriptors is described in the paper: K. Sudars, "Face Recognition Face2vec Based on Deep Learning: Small Database Case". This paper is accepted by the journal "Automatic Control and Computer Science" (included in the SCOPUS database) and will be published in the beginning of the year 2017. Main ideas and results presented in this publication are described below.

4.2.1.1 Face image descriptor

Construction of a facial image descriptor based on deep learning is considered to be the best approach to the face recognition task. Calculation of vectors

embedding visual face features in image and automatically extracted by the artificial neural network (ANN) is considered. In such a way, the comparison of two facial images can be done by calculation of vector distances or correlation coefficients. Related work in some variations can be found in papers representing the top achievements in facial image recognition ([1, 2, 3]). The considered approach is universal and can be applied to many tasks. Here it is used with facial images for person identification problem.

The way of obtaining feature vectors for description of facial images (or any other object in images) consists of two stages: (1) ANN is trained for identification of a person using training data set, (2) ANN gets cropped by removing the linear classification layer (the last layer) and the output of this modified ANN is used as a feature vector or so called facial image descriptor. The process is shown in Figure 4.2.1.

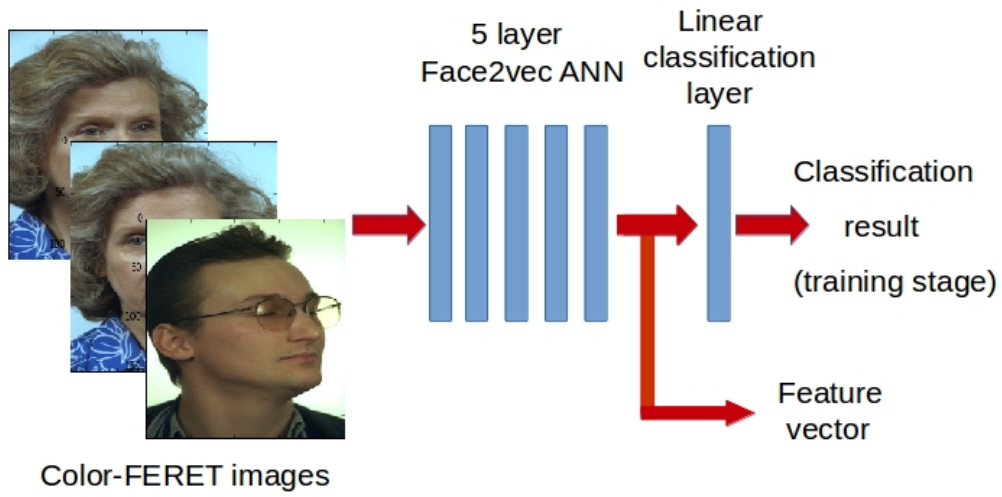

Figure 4.2.1: Feature vector calculation using ANN.

In our project, ANN was trained and tested using the Color-FERET facial image data set [4]. The given task was accomplished using the High Performance Computing (HPC) server with Nvidia K40 GPU running Ubuntu 14.04 and the TensorFlow machine learning software library [5].

4.2.1.2 Artificial neural network ANN architecture and training

For the project experiments, the considered ANNs are trained and tested using the Color-FERET facial image data set. Color-FERET facial image database

consists of approximately 10 000 images (approximately 1000 different people with approximately 10 images per person taken from different views). For research, the classes (representing particular person in the set) of Color-FERET data base are divided into the training set and the validation set in proportion 90:10. Images from the training set are used only for the construction of the descriptor and the validation set of images is used only for validation of the constructed descriptor (for each image within the validation set we find the most similar image from the rest of the validation set using the correlation coefficient of facial image descriptors; it is the most likely that the closest images (featuring higher correlation coefficient) in the validation set belongs to the same class i.e. to the same person). Correlation coefficient shows similarity between objects and their features. It allows to find class members or specific objects in many images. Before training of the ANN, the images are converted to 224x224 pixel resolution.

The considered artificial neural network architecture is shown in Fig.4.2.2. This architecture is close to that of the AlexNet [6]. It consists of five layers of a convolution neural network (CNN) and at the end of each CNN layer stands ReLU (Rectified Linear Unit) nonlinear function. Maximum Pooling layers are used between some CNN layers; they are picking out maximum values from the data. These layers allow to reduce data dimensions and decrease required computational power.

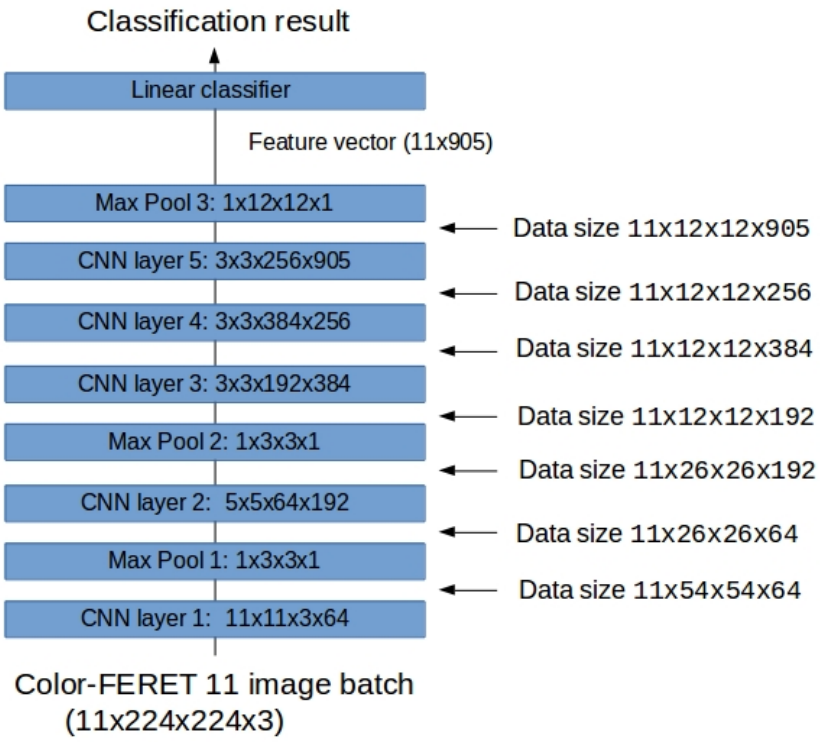

Figure 4.2.2: Artificial neural network for the calculation of facial descriptors.

During the training, ANN coefficients are found using the Stochastic Gradient

Descent (SGD) optimization method that is implemented in the TensorFlow machine learning library. Mean Square Error is used as the minimization cost function, forcing ANN model to converge and making it able to classify images of the training set.

After training, the representative feature vectors of facial images obtained at the output of the trained ANN model. These vectors are normalized and compared to recognize the same person in images by calculating correlation coefficients or Euclidean distances.

4.2.1.3 Experimental results

Two ANN models are trained and validated using the Color-FERET data set: ANN-1 and ANN-2. To achieve ANN model convergence within the training set is not always an easy task. It is further discussed in paper: K. Sudars, "Face Recognition Face2vec Based on Deep Learning: Small Database Case". ANN-1: After approximately 6 epochs, the ANN model No.1 (ANN-1) reaches 98% of accuracy on training set and do not converge to maximum 100% value (learning rate LR is 0.01). It could be acceptable if a training set contains mistakenly labeled data. However, in the case of Color-FERET database, the 100% accuracy should be reached.

ANN-2: In a way to force an artificial neural network to reach 100% accuracy, fine-tuning with much smaller learning rates (LR is 0.0001) was performed (thus obtaining ANN-2 model). As a drawback, it increases training time.

After the training stage, classification accuracy is estimated on the Color-FERET validation set by counting successfully recognized images and dividing the result by the number of all images in the validation set.

The experimental results are shown in Table 4.2.1. Also, the ANN models are tested on frontal face images taken from Color-FERET validation database (named Color-FERET-fa-fb). As it can be seen, it provides better accuracy.

Table 4.2.1: Experimental results

	ANN-1 model, Color-FERET database	ANN-2 model, Color-FERET database	ANN-2 model, Color-FERET-fa-fb database
Accuracy of class (person name) recognition at the first attempt, [accuracy, %]	52.27	87.54	93.94
Accuracy of class recognition within 2 attempts, [%]	68.51	94.87	95.96
Accuracy of class recognition within 3 attempts, [%]	77.02	96.97	**97.98**

4.2.1.4 Conclusions

For object visual recognition in images, the universal approach based on deep learning is used and tested, which is applicable in recognition of all kind of objects and situations. Obtained results lead to the following conclusions: (1) ANN fine-tuning from 98% to 100% accuracy on the training set using super small learning rates (smaller than 0.0001) can significantly improve the accuracy of face recognition system (however, it increases training time); (2) the proposed ANN architecture under described training conditions is capable to represent necessary features for face recognition. During experiments the best trained ANN model achieves 94% accuracy on Color-FERET frontal face image database. Further development: it is expected that better results could be obtained if ANN would be trained on much larger data set like [7].

4.2.2 Generation of the training data for RNN- based object detector

In the previous period of the GudPils project, a method for detection of moving objects was developed. The method allows to detect those objects in the frame that cross a virtual detection line (a single row of pixels). Pixel values form this detection line are processed by recurrent neural network. The network returns the number of moving objects on the detection line at the current frame based on the information form the current and few previous frames. Since the method is based on supervised machine learning, it demands a large training dataset with correct labels. Since the method is original, such labeled datasets for this particular task are not ready available on the Internet unlike the datasets for more common computer vision tasks (image classification, face recognition). Manual labeling of data that was proposed in the previous period of the project is slow and offers minor scientific contribution. Therefore, in this period of the project we targeted methods for faster generation of labeled data.

4.2.2.1 Semi-automatic data labeling

We developed a data labeling application that automatically tries to label the training data and allows users to correct the mistakes of automatic labeling using a graphical user interface. First part of the proposed method is automatic labeling, which does not require the label input from a human. This task is different from the task of the final object detector. While the final system will have to classify current frames based on the few previous frames, the automatic labeling of training data has an access to all the frames in the video (the whole spatio-temporal image is available).

At the start of the labeling program, the proposed GUI (figure 4.2.3) displays the first frame of the video. The user defines the detection line in the frame with two clicks of a mouse (marking the endpoints of the line). The first frame of a video is used to create an initial background line that corresponds to the empty detection line. If some moving objects are already on the detection line in the

first frame, user is advised to fast forward the video by pressing any key on the keyboard (except the "e" key). When there are no moving objects on the detection line, pressing of "e" will start the automatic labeling procedure.

The detection line of the current frame is subtracted from the background line. The absolute value of this difference becomes a row in a new spatio-temporal image. The width of this spatio-temporal image is equal to the length of the detection line. The height of this image will be equal to the number of frames in the input video. In the GUI (see 4.2.3) user can observe the creation of the spatio-temporal image of absolute difference between the current line and the background line. The second observable spatio-temporal image is obtained by thresholding a difference line with a single threshold. This visualization of acquired spatio-temporal images can be disabled for faster processing of video.

Figure 4.2.3: The first window of semi-automatic labeling GUI

Initially, the background line is equal to the line of the first processed frame. Later, background line adapts to the changing conditions in the video. If less than 20% of pixels on the current thresholded line are white, the background line is updated using the formula [4.2.1]. Otherwise, the background line is not updated since it likely contains some moving objects.

$$line_{new\_background} = line_{old\_background} \cdot 0.95 + line_{current} \cdot 0.05 \tag{4.2.1}$$

When all frames are processed, the acquired spatio-temporal threshold image undergoes further processing in order to reduce the impact of noise. The morphological closing with a kernel of size $(3, 3)$ is followed by morphological opening with kernel $(5, 5)$. Further, values of all zero pixels surrounded by pixels with value 1 are changed to be 1.

The processed spatio-temporal threshold image is then automatically labeled. Continuous white regions are detected in each row of this image. The label of each row is equal to the number of continuous white segments on this row that are longer than 10% of the length of the whole row.

The described automatic stage of labeling method does not consume human time, but it is also less accurate than manual segmentation. Therefore, the next step consists of a GUI (figure 4.2.4) which allows easy detection and correction of errors made in the automatic stage. Fig.4.2.4a depicts a region of spatio-temporal image which was successfully labeled by the automatic process. Each blue line in the figure depicts a frame at which the label on the detection line changes. The number under each dividing line is the according label for the rows under this line (until the next dividing line).

The proposed GUI for labeling of the rows allows user to scroll through the whole labeled spatio-teporal image. In Fig.4.2.4b, another region of spatio-temporal image is depicted. In this region, the automatic labeling has made two errors pointed out by the red circles (these circles are not part of the GUI). In such situations GUI allows user to make corrections. The error at the top of the image can be corrected by pointing the cursor of the mouse to the desired position of the line with label "0" and clicking the right mouse button. If the right button is clicked, and the closest line to the cursor is the line above the cursor, this closest line changes its position to the position of cursor. Conversely, if the closest line is located below the cursor, then this line is deleted. The labels under the deleted line become equal to the labels above this deleted line. Therefore, in order to correct the second mistake of automatic labeling, the user has to point the cursor close and above the line with label "1" and click the right mouse button. In the concrete situation of Fig.4.2.4b, two lines will disappear. Since all labels under the line with label "1" will become "2", the next line that divided region of labels "1" and labels "2" becomes redundant and is automatically removed. The manually corrected labels are shown in Fig.4.2.4c.

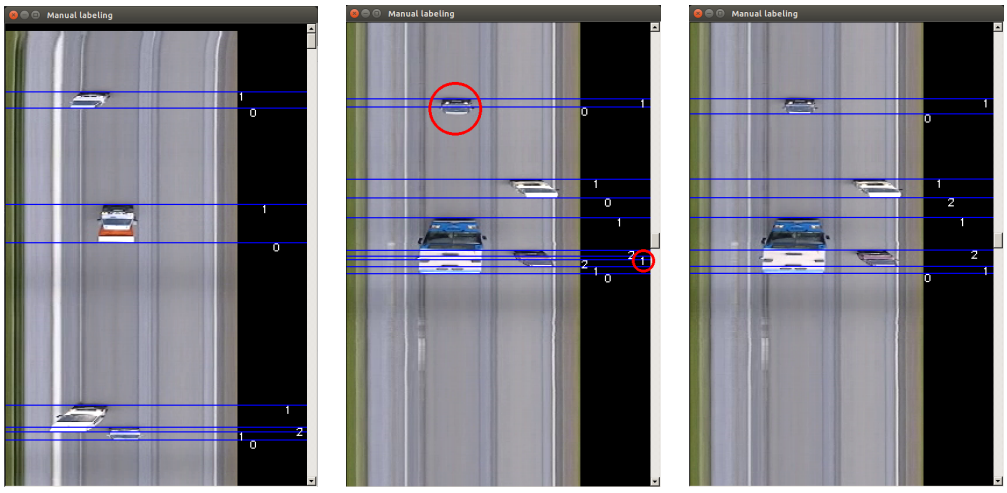

(a) (b) (c)

Figure 4.2.4: GUI for inspection and correction of errors of automatic labeling

The labeling GUI offers one more error correction possibility. When a new dividing line needs to be added, user can press a number on the keyboard that corresponds to the label that the user wants to add. Then a click of the left mouse

button will add a new dividing line at the position of a cursor. When the user has inspected and corrected the whole spatio-temporal image, labels are one-hot encoded as vectors and saved to the hard drive along with the spatio-temporal image.

The proposed GUI was implemented in Python language using *numpy*, *cv2* and *PyQt4* libraries.

4.2.2.2 Training data generation using a game engine

The semi-automatic labeling of training data is faster than fully manual labeling; however, it is still time consuming when large training sets are required. The proposed object detection method is based on deep supervised machine learning, which depends on the availability of large amounts of labeled data. This was shown by the success of Convolutional Neural Networks (CNN) on the image classification task that was partially enabled by the creation of ImageNet - a large database of labeled images [8]. Thus, the creation of new labeled datasets is an important area of research and a necessary prerequisite to extend the applicability of DL algorithms. For example, a Visual Genome [9] dataset allows training of systems that can not only classify images, but also describe and answer questions about objects and their relations in these images. The creation of ImageNet and Visual Genome involved the use of Amazon's Mechanical Turk which is a crowdsourcing platform. Such platforms allow to carry out large-scale labeling of data by dividing the work in to smaller tasks and employing many humans without expert knowledge in the computer vision field. The above mentioned projects created datasets that are useful for different popular computer vision tasks. However, these datasets are not suitable for the specific object detection method that was developed in current project. Conducting of large original data labeling work aimed at the specific detection method would not only be time consuming, but also would bring little benefit to the field.

Another approach to deal with the lack of labeled data is to train the Deep Learning models on synthetic data. Vision tasks can benefit from increasingly realistic computer-generated imagery, where each object has a defined label and coordinate in the 3D scene. For example, in [10] authors used 3D game engine to create scenes with towers made of blocks. Physics simulation determined if the tower would fall. CNN was trained on synthetic images of the towers and learned to distinguish stable and unstable towers. Tests proved that this trained network was able to also predict stability of real block towers in images. In this and similar work [11], the simulated objects were simple rectangular blocks. One of the intended objectives of this project is to go beyond simple object simulations, as was also done in [12]. The more lifelike synthetic data generated by modern game engines can prove to be a viable resource of labeled data for practical computer vision tasks. In such case, an important obstacle for further success of machine learning in computer vision would be overcome.

In order to test the idea that our detection algorithm can be trained with synthetic data and that this data is a valid substitute for the real labeled data, we begun with a simplified task. In this task, the trained object detection system

had to count marbles that are crossing the detection line. The proposed object detection method requires training data in the form of a spatio-temporal images. Each row of such image must have an appropriate label. In order to synthetically generate such spatio-temporal images, we created a simulation environment in the *Unreal Engine 4* game engine.

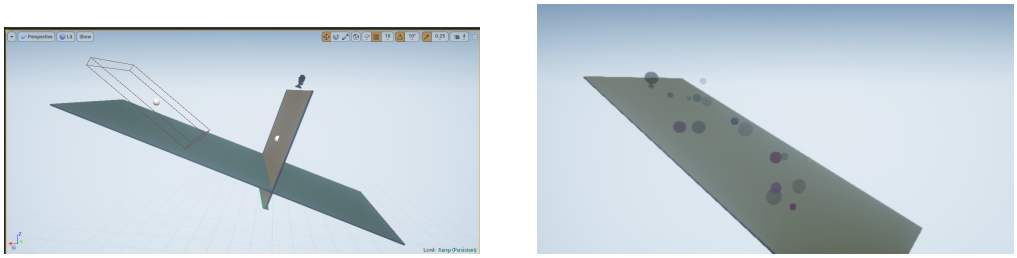

(a) (b)

Figure 4.2.5: Simulation environment for training data generation using Unreal Engine 4.

The simulation environment (Fig.4.2.5a) consists of a tilted plane that will be the background of the spatio-temporal training image. The R, G, and B components of the color of this plane smoothly change in time, so that training data will include backgrounds with different colors and intensities. The transparent rectangular box above the background plane is a spawn volume. At any position within this box, a sphere can be generated. Thus, the spheres with random positions, colors, opacity, and sizes are generated over the background plate at random time intervals. Simulated gravity pulls the spheres downwards, so they collide with the background plane and continue to move over the surface of the plane in the direction of its slope. When the spheres roll off the background sphere, they are eliminated. Fig.4.2.5b shows a frame from a running simulation where several spheres are already generated and are rolling down the background plane.

In order to increase the variance in the training data, the simulated environment also includes changing lighting. The direction and intensity of the lighting changes smoothly in a random direction, while the color of the light can make small random jumps in the color space.

The simulation also includes a plane that is perpendicular to the background plane. It is also perpendicular to the movement direction of the spheres. This plane is located to be in the way of spheres; however, this plane not collide with the spheres, so the spheres freely move trough it. However, this plane detects each occurrence of its overlap with the spheres. Thus, this plane can detect how many spheres are overlapping with it at each frame. Thus, the number of overlapping spheres at each frame is saved to a text file and corresponds to the training labels for the current frame. Thereby, the detection plane in the game engine environment fulfills the same function as the detection line in the proposed object detection method. Although, in the simulation environment the detection result is always correct.

In order to acquire the frames for the formation of spatio-temporal image, a camera is inserted in the simulation environment. This camera is positioned perpendicular to the detection plate. Figure 4.2.6a shows the view from the camera. Because of the positions of camera and detection plane, the plane appears as a line in the field of view of the camera. The detection plane is not visible in the final rendering of the frames and is used only to obtain the labels for each frame. The frames from this camera are saved along with the labels.

The proposed simulation generates frames and according labels which are then processed to prepare the final spatio-temporal image and one-hot coded labels. Since the detection plane in the simulation environment splits the camera frames precisely at the middle row of the frame, only this row is used to create the final spatio-temporal image. The fragment of synthetically generated spatio-temporal image is shown in the figure 4.2.6b.

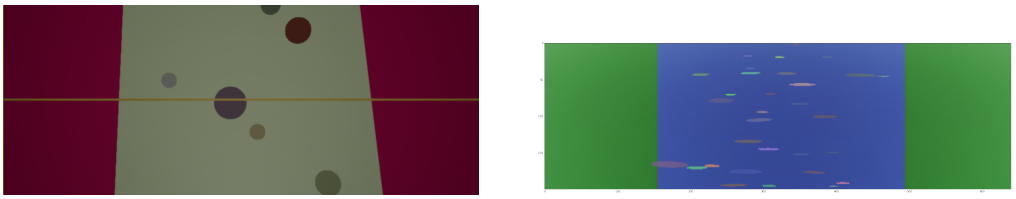

(a) (b)

Figure 4.2.6: Synthetic data generated in Unreal Engine 4.

4.2.3 Summary

The following results obtained within the review period number 3 can be emphasized:

1. The technique of image descriptor for unique object description with one vector was explored. For this purpose, human facial images were considered and processed based on artificial neural networks. The trained ANN model converts any image with face into a feature vector, which can be compared to another vector by calculating a correlation coefficient. Experiments show that the trained ANN achieves 94% accuracy on COLOR-FERET frontal image subset. It is described in more details in the paper K. Sudars, "Face Recognition Face2vec Based on Deep Learning: Small Database Case" accepted by the journal "Automatic Control and Computer Science" included in SCOPUS database;

2. Interdisciplinary "Baltic Electronics Conference 2016" was attended and the paper presented. It was prepared in collaboration with colleagues from other projects: K. Sudars, I.Bilinskis, E.Buls, "Discrete Fourier Transform of the signals recovered by using high-performance Event Timers".

3. In order to acquire labeled data for the moving object detector, two approaches were investigated. One of the approaches resulted in a method

and an application for semi-automatic labeling. In this approach an algorithm performs fast but sometimes erroneous labeling. Then a human is presented with a GUI that allows convenient error correction. The second approach was based on the generation of synthetic data using a game engine. Using this engine, simplified environment with moving spheres was developed. This simulation will allow to generate large amount of labeled data which in turn will allow to decide if this approach of data generation is promising for more complex environments.

Chapter 4.3

EDI REMSENS group: Investigation of possibilities to use remote sensing data for solving city security tasks

During the third reporting period, activities of the REMSENS group were focused on the following tasks related to exploitation of remote sensing data in smart cities:

- urban land use and vegetation mapping for the GIS system with changes in time;
- development of the algorithm for simulation of territory flooding using the surface height model formed from LiDAR data;
- elaboration on informative band selection methods for hyperspectral image classification.

Two first activities were aimed at development of practicable solutions, the third activity continued theoretical studies related to hyperspectral image classification.

4.3.1 Urban land use and vegetation mapping

Activities within this task are oriented towards accumulation of necessary knowledge and development of practical tools for detection of vegetation changes in urban and suburban areas that can be used by municipalities to monitor situation in that respect. During the reporting periods, sample images from Sentinel-2 were explored to reveal their properties and potential problems related to dynamic mapping of vegetation changes. For the current task have been used two Sentinel-2 images of Riga Fig.4.3.1. One image was taken on 28^{th} August, 2015 and the other on 10^{th} September, 2016.

Figure 4.3.1: Sentinel-2 images of Riga.

Normalized Difference Vegetation Index (NDVI) [[13]] is a simple indicator that can be calculated from multispectral images to assess whether the target being observed contains live green vegetation or not. To determine the density of green vegetation on a patch of land, we must observe the distinct wavelengths of red and near-infrared light reflected by the plants. The pigment in plant leaves, chlorophyll, strongly absorbs visible light (from 0.4 to 0.7 μm) for use in photosynthesis. The cell structure of the leaves, on the other hand, strongly reflects near-infrared light (from 0.7 to 1.1 μm). The more leaves a plant has, the more these wavelengths of light are affected, respectively. In general, if there is much more reflected radiation in near-infrared wavelengths than in visible wavelengths, then the vegetation in that pixel is likely to be dense and may contain some type of forest. If there is very little difference in the intensity of visible and near-infrared wavelengths reflected, then the vegetation is probably sparse and may consist of grassland. NDVI is calculated using the formula:

$$NDVI = \frac{NIR - RED}{NIR + RED}$$

, where NIR is the image of the near infrared spectral band and RED is the image acquired in red visible light region. Calculations of NDVI for a given pixel always result in a number that ranges from minus one (-1) to plus one (+1);

however, no green leaves gives a value close to zero. A zero means no vegetation and close to +1 (0.8 - 0.9) indicates the highest possible density of green leaves [`http://earthobservatory.nasa.gov`]. After calculating NDVI values for both images, a threshold was applied to replace image of multiple shades of grey with pseudocolor image. Pixel is marked red if its NDVI is less than 0.2, marked green, if NDVI exceeds 0.55, otherwise it is marked blue. The results are illustrated in Fig.4.3.2. We can see that vegetation levels have increased,

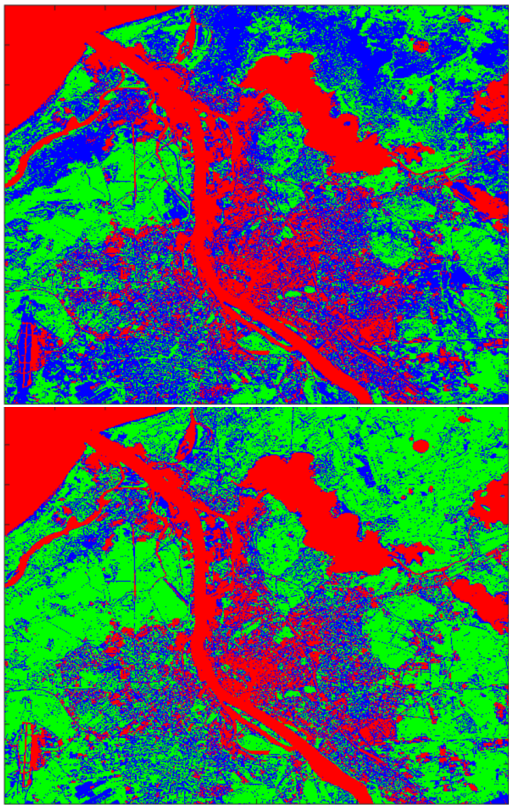

Figure 4.3.2: NDVI pseodocolor images of Riga.

as areas which were mostly colored blue in 2015's image are green in 2016's image. One of the explanations for this change is that in the hot summer of 2015 the grass was partially withered. To further analyse vegetation changes, a difference of NDVI's was calculated and displayed as another pseudocolor image (see Fig.4.3.3): pixel is marked black if both NDVI's are less than 0.2 (no vegetation in both images), marked green if NDVI is increased by more than 0.1, marked red if NDVI is decreased by more than 0.1, otherwise it is marked blue. Some areas that showed increased vegetation in thresholded NDVI are marked blue now indicating vegetation has no noticeable changes. Explanation is that vegeation increase is small (therefore unnoticeable in current image) but large enough to cross NDVI threshold. The mapping of land use was based on the Bayes classifier that uses Gaussian distribution. The main problem here was acquiring ground truth data for deciduous trees and bushes (see Fig.4.3.4).

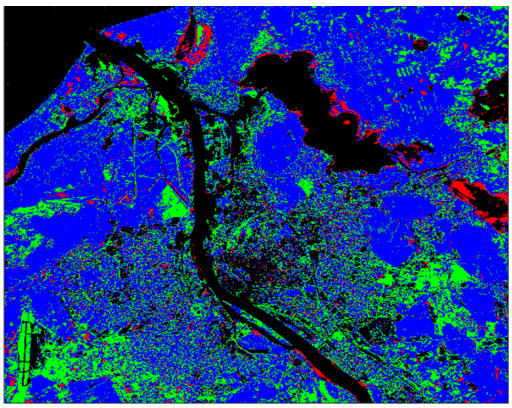

Figure 4.3.3: Vegetation difference

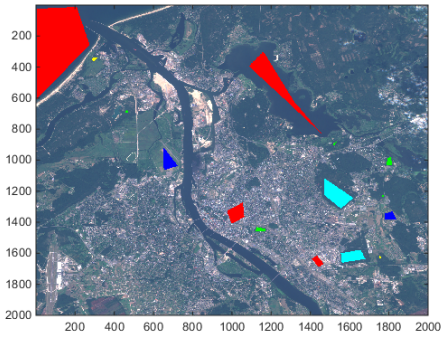

Figure 4.3.4: Ground truth samples.

Vegetation classification results are shown in Fig.4.3.5 and visualized in Fig.4.3.6. Deciduous trees are marked green, conifers - light blue, grasslands - dark blue, bushes - yellow and areas without vegetation are red.

As only ground truth areas were classified, accuracy is high but not really informative. More interesting is to compare classification results between both images presented in Fig.4.3.7. It is noticed that the same vegetation categories are obtained for approximately 80% of ground truth pixels. Further classification experiments with more ground truth data are planned to reveal error sources and increase classification stability between different time instances.

4.3.2 Algorithm for simulation of territory flooding

During the reporting period, studies were continued related to creation of a practical tool for simulation of flooding on the basis of LiDAR elevation data. The following main activities should be mentioned:

- filling the holes in elevation image related to missing LiDAR data;

24.08.2015			Classified as:			
	Deciduous trees	Conifers	Grassland	Bushes	No vegetation	
Deciduous trees	86%	2%	0%	12%	1%	
Conifers	6%	92%	0%	1%	1%	
Grassland	0%	0%	100%	0%	0%	
Bushes	7%	5%	0%	88%	0%	
No vegetation	0%	0%	0%	0%	100%	
				Overall accuracy, %		98,8%

10.09.2016			Classified as:			
	Deciduous trees	Conifers	Grassland	Bushes	No vegetation	
Deciduous trees	91%	1%	1%	6%	1%	
Conifers	7%	93%	0%	0%	0%	
Grassland	0%	0%	100%	0%	0%	
Bushes	5%	7%	0%	89%	0%	
No vegetation	0%	0%	0%	0%	100%	
				Overall accuracy, %		98,9%

Figure 4.3.5: Vegetation classification accuracy.

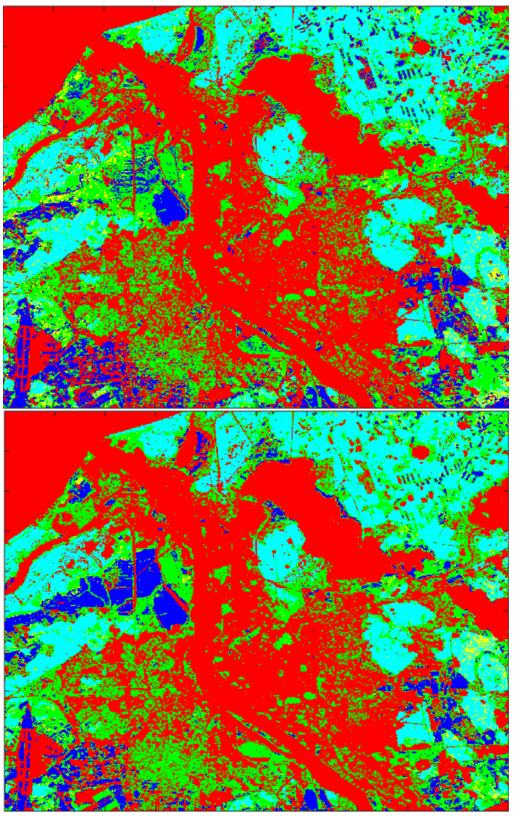

Figure 4.3.6: Vegetation classification results.

		10.09.2016					
		Deciduous trees	Conifers	Grassland	Bushes	No vegetation	
24.08.2015	Deciduous trees	75%	6%	8%	2%	9%	
	Conifers	8%	87%	0%	4%	1%	
	Grassland	34%	0%	48%	0%	18%	
	Bushes	35%	43%	1%	20%	1%	
	No vegetation	11%	1%	0%	0%	87%	
					Overall accuracy, %		79,4%

Figure 4.3.7: Classification accuracy between years 2015 and 2016.

- developing algorithm for simulation of flooding due to the rise of the water level;
- creation of a software tool implementing LiDAR data processing and flooding simulation.

The elevation model developed from LiDAR data during the previous reporting period misses data for water basins as LiDAR fails to detect reflections from water. To facilitate simulations of water level and its rise, it is necessary to fill in these holes with real elevation data from the sea level. Fig.4.3.8 shows the elevation model created from LiDAR data with missing data represented by white color.

Three different types of "holes" were considered, namely 1)lakes, 2)rivers and 3)other. We define a lake as a water basin (object of connected pixels with missing elevation data) that is characterized by expected equal elevation above the sea level of all pixels. To fill in elevation data for lakes, the following procedure was proposed:

- interactively choose a point within the lake on the image;
- delineate a lake object around the chosen point and ask for confirmation. This step is needed to ensure that the lake object does not extend to connected rivers that fall into lake or flow out of it. If such happens, a tool for drawing a border between the lake and the river should be used;
- find the coast pixels closest to the lake using the morphological dilation of the binary lake object.
- collect elevation data from coast pixels;
- calculate elevation of the lake above the sea level and fill in the lake object with this number (equal for all lake pixels). Within this step, it is proposed to choose an elevation value of the lower coast pixels, dismissing 2 percent "outsiders".

More sophisticated procedure is needed to fill in river objects as the elevation of river pixels is different. We define a river as a water basin (object of connected pixels with missing elevation data) that is characterized by expected

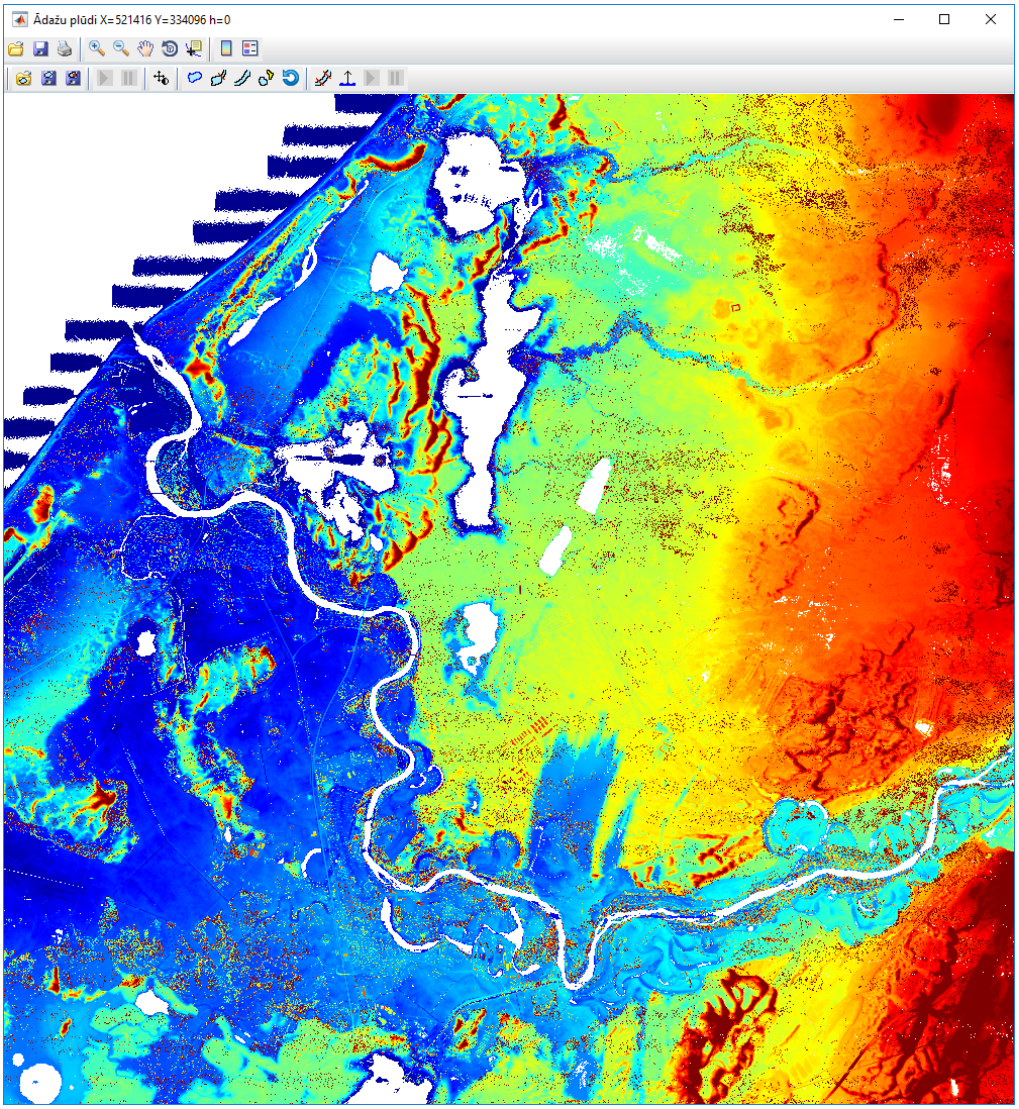

Figure 4.3.8: Elevation model of river Gauja region created from LiDAR data. Spatial resolution is 1m, elevation range from 0 to 20m.

rising elevation above the sea level from pixels closer to the sea to pixels farther from the sea (distance calculated by the centreline of the river flow). To fill in elevation data for rivers, the following procedure was proposed:

- interactively draw a centreline of the river by selecting points within the river object on the image, starting from points closer to the sea;
- delineate a river object around the chosen points;
- assign maxRadius = 0;
- calculate elevation of each selected centreline point as follows:

  - draw a circle surrounding the centreline point that contains at least 1/4 pixels with elevation data availablee (coast pixels). To achieve that, iterate with a growing radius. If the radius used is greater than maxRadius, set new maxRadius value equal to the radius used;
  - calculate elevation of the centreline point above the sea level as the minimum height of the coast pixel included in the found circle;

- filter the elevation curve of centreline points using a median filter;
- ensure that elevation is not lowering from point to next point upper the river;
- form a detailed centreline with equal (10m) steps between the points;
- calculate elevation of each river pixel above the sea level as the height of the closest detailed centreline point. If the point is farther away from this centreline point than maxRadius*2, exclude that pixel from the river object (it possible relates to the influent river).

Information about the river objects defined by the procedure above should be saved for later use within the flooding simulation.

"Other" objects are filled in after lakes and rivers by applying the algorithm used for the lakes automatically.

Fragment of the image after filling all objects is shown in Fig.4.3.9.

When the river elevation data are filled in, simulation of flooding due to the rise of the water level in the river can be started. It is based on the assumption that all river pixels are rising with the same increment as the pixel for what the rise is simulated (that is a serious simplification, of course, but to implement a more realistic flooding model, more sophisticated hydrologic model is needed which we are lacking at present). The proposed algorithm is as follows:

- interactively choose a "measurement" point on the river the rise of which will be simulated;
- input a new elevation of the chosen point and calculate the increment in respect to the original value;
- form a new elevation model of the flooded river by raising the elevation of each river pixel by the same amount as the "measurement" pixel;
- iterate to simulate flooding of nearest coast pixels:
  - find the current unflooded coast pixels using the morphological dilation of the current binary river object;
  - add coast pixels to the flooded river object if they feature lower elevation than the neighboring water pixels and set their elevation values to that of the higher neighboring water pixels;
  - visualize the new instance of the flooding river;

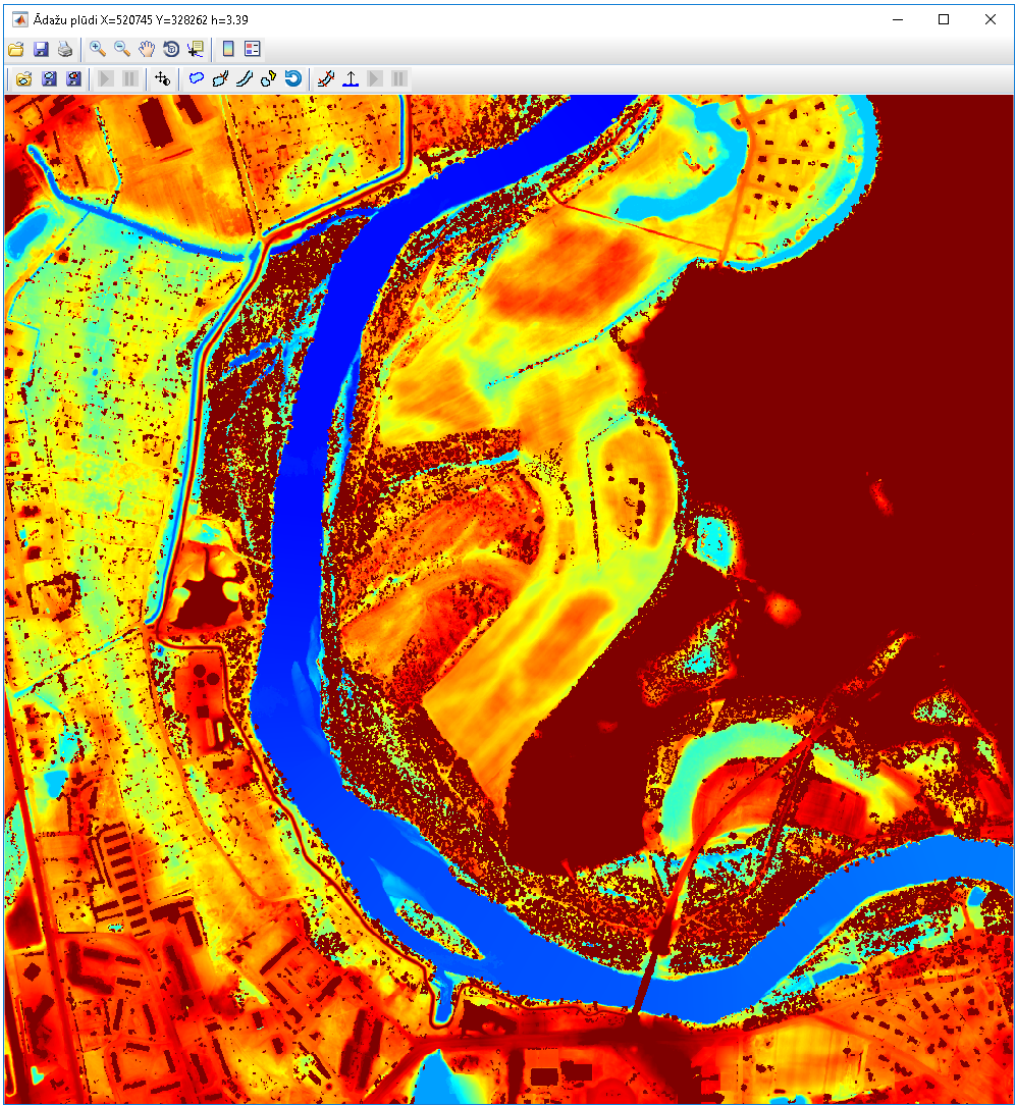

Figure 4.3.9: Elevation model of a fragment of river Gauja near the bridge from Adazi to Kadaga after filling all water objects, elevation range from 0 to 6m.

– finish iterations if no new flooding river pixels are detected.
Fragment of the image with simulated flooding is shown in Fig.4.3.10.

Software tool for visualisation of possible flooding on the basis of such model was developed in MATLAB and compiled to standalone executable for Windows systems. The tool implements the following functions partially described above:

- open model / save model / save fragment;
- visualize elevation by color / adjust height range;
- fill missing elevation data for lake / river / other objects / undo last filling operation;

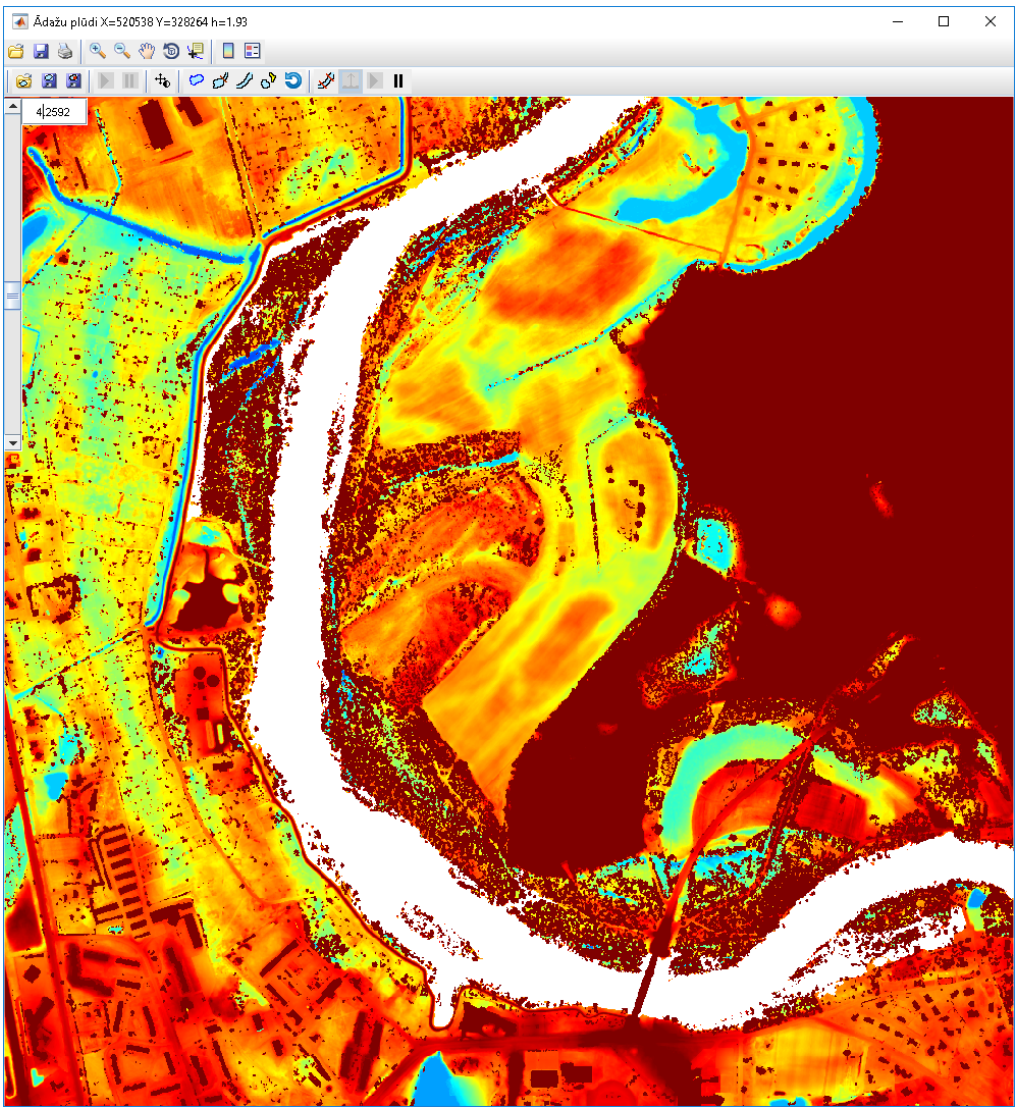

Figure 4.3.10: Elevation model of a fragment of river Gauja near the bridge from Adazi to Kadaga after simulation of a rise of the water level by 3m. Flooded river indicated by white color, elevation range from 0 to 6m.

- delimit water objects by drawing a line between two points and calculation of elevation values along this line using interpolation;
- simulate rise of the water level in river / pause and resume simulation / delimit a river fragment for the simulation of flooding.

This tool will be demonstrated to interested municipalities for potential practical use. During the next period, an attempt to speed up flooding simulation will be made and possibilities to implement a more sophisticated hydrological model explored.

4.3.3 Selection of informative bands for classification of hyperspectral images

Theoretical studies on selection of informative bands for classification of hyperspectral images were continued. Results of previous research were presented in BEC-2016 conference and described in corresponding paper (see Appendix 4.1). Further studies of this topic led to new results and deeper elaboration on this topic, a paper describing them is in preparation (Appendix 4.2).

Chapter 4.4

EDI RADAR group: Development of the ultra-wideband technology and UWB-based systems for security monitoring

The following tasks were considered during the period 3:

1. Experimental tests of signal processing methods for detection of changes in a room, object displacement
2. Improvement of UWB radar sensor functional parts to increase range.

Experimental radar sensor application tests were performed and signal processing methods examined within the scope of the first task. Second task was oriented on improvement of radar sensor prototype hardware.

4.4.1 Experimental tests of signal processing methods for detection of changes in a room, object displacement

In this section, signal processing methods for detection of changes in radar sensor reflected signals that are caused by object movement and room changes are presented. The experimental tests were made using Radar group's self designed UWB radar sensor hardware modules (transmitters, antennas) and using an wideband (20 GHZ) real-time oscilloscope as the receiver or using experimental, multi-channel radar sensor prototype based on equivalent time sampling principle.

4.4.1.1 UWB sensor signal processing for object tracking

In UWB system for object tracking one transmitter, located at coordinates (x_T, y_T), radiates UWB pulses, which after reflecting from objects O_m, $m = 1, 2, \ldots$, located at (x_{O_m}, y_{O_m}), are received by multiple UWB receivers Rx_n, $n = 1, 2, \ldots$, located at coordinates (x_{R_n}, y_{R_n}). The signal processing task is to find the coordinates of the objects given the signals $s_{R_n}(t)$ at the receivers (Fig. 4.4.1).

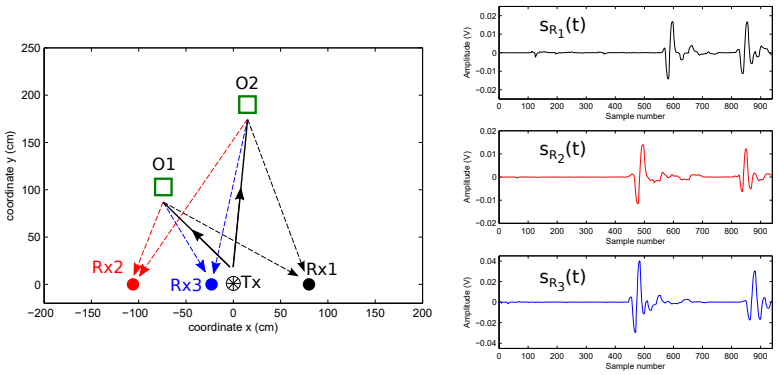

Figure 4.4.1: Paths of UWB pulses after being radiated by UWB transmitter Tx – the pulses are reflected from objects O_1 and O_2 and received by UWB receivers Rx_1, Rx_2 and Rx_3 producing the signals $s_{R_1}(t)$, $s_{R_2}(t)$ and $s_{R_3}(t)$, respectively (a background signal, which is composed of a direct pulse (coming from Tx to Rx_n) and reflected pulses from the walls and other static objects is excluded, since it is known and can be obtained when objects are not present).

In order to calculate positions of the objects, the following steps are performed.

1. The time instants t_{mn} of the received reflected UWB pulses are found and the corresponding distances Tx-O_m-Rx_n are calculated as $L_{mn} = (t_{mn} - t_0)c$, where t_0 is the time instant when pulses are radiated and c is the speed of light in vacuum.

2. Given the coordinates of the transmitter and receivers and the corresponding distances L_{mn}, the equations of ellipses are obtained:

$$A_{mn}x^2 + B_{mn}xy + C_{mn}y^2 + D_{mn}x + E_{mn}y + F_{mn} = 0, \tag{4.4.1}$$

where the coefficients A_{mn}, B_{mn}, C_{mn}, D_{mn}, E_{mn} and F_{mn} are determined by coordinates (x_{O_m}, y_{O_m}) and (x_{R_n}, y_{R_n}) and the corresponding distances L_{mn}.

3. Given the equations (4.4.1), the intersections of ellipses are found by solving the systems of two equations:

$$\begin{cases} Ax^2 + Bxy + Cy^2 + Dx + Ey + F = 0 \\ \hat{A}x^2 + \hat{B}xy + \hat{C}y^2 + \hat{D}x + \hat{E}y + \hat{F} = 0, \end{cases} \tag{4.4.2}$$

where A, B, C, D, E, F and $\hat{A}, \hat{B}, \hat{C}, \hat{D}, \hat{E}, \hat{F}$ are the coefficients A_{mn}, B_{mn}, C_{mn}, D_{mn}, E_{mn} and F_{mn} with different indices mn and $\hat{m}\hat{n}$.

4) After solving the systems of equations, all the intersections are obtained and analyzed to find the positions of the objects. An illustrative example of this procedure when 3 receivers are used is shown in Fig. 4.4.2.

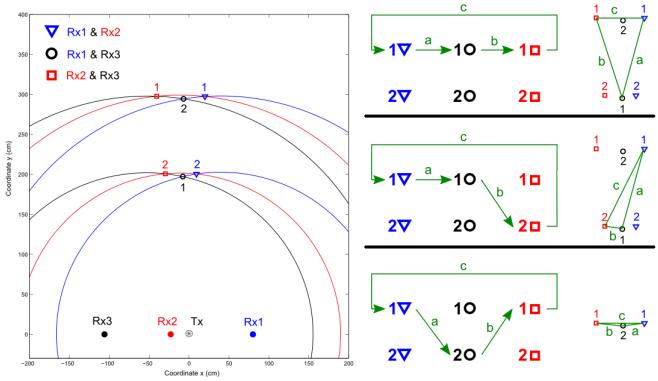

Figure 4.4.2: Intersections of differently colored ellipses corresponding to Rx1 (blue lines), Rx2 (red lines) and Rx3 (black lines), and 3 combinations of their interconnections (triangles on the right side) obtained by using the graph (in the middle part) consisting of all the differently marked intersections.

In Fig. 4.4.2 the blue triangles are intersections of the ellipses corresponding to receivers Rx1 (blue lines) and Rx2 (red lines), the black empty circles are intersections of the ellipses corresponding to Rx1 (blue lines) and Rx3 (black lines), while the red squares are intersections of the ellipses corresponding to receivers Rx2 (red lines) and Rx3 (black lines). By using the graph as shown in the middle part of Fig. 4.4.2, these differently marked points can be interconnected to form all the possible triangles the vertices of which conform to the intersections of differently colored ellipses (in this example only three combinations are shown). If the lengths of at least two edges (a, b or a, c or b, c) are less than a predefined threshold value, then it is assumed that the three intersections which are the vertices of the triangle, correspond to one object, the position of which is assumed to conform to the centroid of the triangle as shown in Fig. 4.4.3.

Experimental results. The first experiment was carried out by using one Tx and two Rx antennas, and the object was a 1m×1m metal plate which was placed on a straight line perpendicular to the line connecting the antennas at the distance of 0.6m and increasing by 0.2m up to 3m from Tx. The obtained localization results are shown in Fig. 4.4.4 and correspond well to the real positions of the object as it produces strong reflections and peaks of the received pulses can be clearly distinguished.

The second experiment was carried out by using the same antennas, but the object was a person that was approaching and then moving away from Tx in the same straight line. The obtained positions are shown in Fig. 4.4.5 with the dots getting darker as time progresses. The obtained signals at both receivers are shown on the right side with the red line representing the location of a global maximum point in each signal. As it follows, the positions are more precise

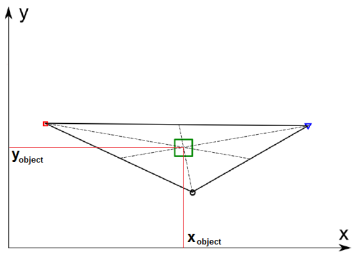

Figure 4.4.3: Position of the found object at the centroid of triangle the vertices of which conform to differently marked intersections of ellipses corresponding to Rx1, Rx2 and Rx3 and the lengths of two edges of which are less than a predefined threshold value.

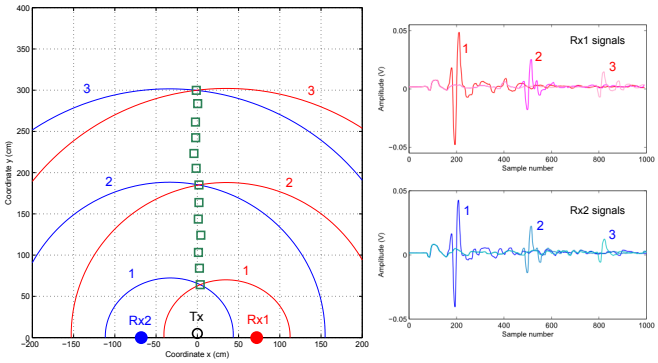

Figure 4.4.4: Localization result of the metal plate placed on a straight line perpendicular to the line connecting the antennas at the distance of 0.6m and increasing by 0.2m up to 3m from Tx (the signals on the right side are obtained at the receivers Rx1 and Rx2 allowing to produce the corresponding ellipses 1, 2, and 3).

at smaller distances from Tx since stronger reflections are obtained, and more noise is produced when the object is located at larger distances from antennas. After reducing the noise by filtering the obtained red lines on the right side of Fig. 4.4.5, the result improves at larger distances as shown in Fig. 4.4.6 (it is noted that all the processing is causal with the output depending only on past and current received signals).

The third experiment was carried out by using one Tx and three Rx antennas, and the object was a person that was moving along a triangular trajectory (anticlockwise). The obtained positions are shown in Fig. 4.4.7 with the points getting darker as time progresses. The first upper figure is obtained when ellipses corresponding to Rx1 and Rx2 are used, the second upper figure is obtained when ellipses corresponding to Rx1 and Rx3 are used, the third upper figure is obtained when ellipses corresponding to Rx2 and Rx3 are used, and the fourth upper figure is obtained when ellipses corresponding to Rx1, Rx2 and Rx3 are

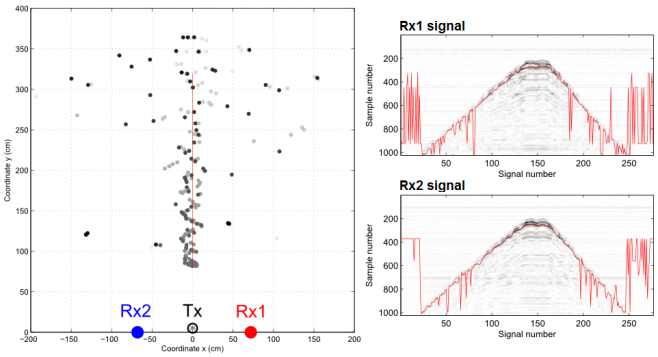

Figure 4.4.5: Localization result of a person approaching and then moving away from Tx in the straight line – the dots (positions) are getting darker as time progresses (the signals on the right side are obtained at Rx1 and Rx2 with the red line representing the location of a global maximum point in each signal).

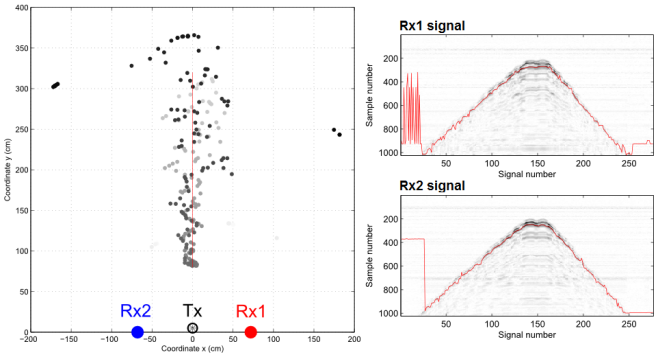

Figure 4.4.6: Localization result of Fig. 4.4.5 after causal filtering of the red lines on the right side of Fig. 4.4.5.

used by combining all the intersections as explained in Fig. 4.4.2. The lower three figures show the obtained signals at the receivers with the red lines representing the estimated locations of reflected pulses in the signals. As it follows from the rightmost upper figure, the calculated positions conform approximately to the real trajectory.

The last experiment was carried out by using one Tx and three Rx antennas, and the objects were two persons approaching and then moving away from antennas at different speeds along straight lines perpendicular to the line connecting the antennas. The obtained positions are shown in Fig. 4.4.8 allowing to conclude that the limitation of the current method is that only one object most closely located to antennas can be detected due to only the first reflected pulses are considered. The problem of detecting and tracking multiple objects will be the topic of further research.

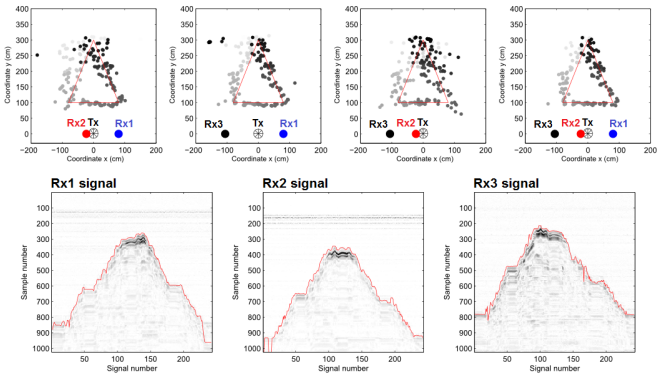

Figure 4.4.7: Localization result of a person moving along a triangular trajectory (anticlockwise) – the dots (positions) are getting darker as time progresses (the lower three figures show the signals at Rx1, Rx2, and Rx3 with the red lines representing the estimated locations of reflected pulses in the signals).

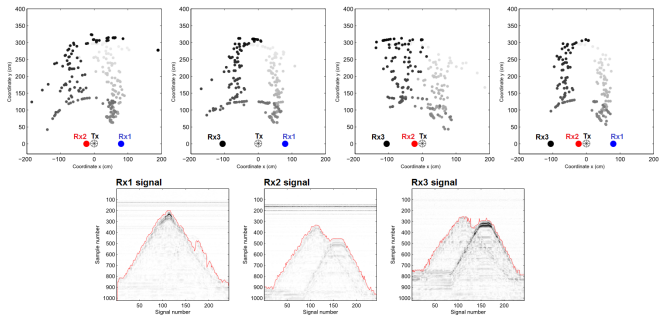

Figure 4.4.8: Localization result of two persons approaching and then moving away from antennas at different speeds along straight lines perpendicular to the line connecting the antennas – the dots (positions) are getting darker as time progresses (the lower three figures show the signals at Rx1, Rx2, and Rx3 with the red lines representing the estimated locations of the first reflected pulses in the signals).

4.4.1.2 Karhunen-Loeve transform as a tool to eliminate signal's redundancy for small target detection

Research on detection of small moving target (object) in ultra-wide band pulse radar sensors systems was carried out. The research aim was to investigate methods of small object movement detection that are masked by large signal reflections from other objects in the area covered by the radar sensor. Karhunen-Loeve transform was used to filter out small object movements from the reflected radar sensor signals. The method was tested on synthesized signals and on signal obtained from experiments. The research results were published in a scientific journal paper presented in Appendix 4.3: *Aristov V. (2016) Karhunen-Loeve transform as a tool to eliminate signal's redundancy, when small targets*

detection. Sciences of Europe. Vol 2, No 2 , 53-57 (in Russian). Journal link [PDF,RU].

4.4.2 Improvement of UWB radar sensor functional parts to increase range

Radars in which short video pulses are used to excite a wideband antenna by pulse excitation method are widely used in the ground-penetrating radar subsurface sounding, remote monitoring of human health, object motion sensors, human detection behind obstacles, search for living beings under the rubble, etc. The excitation pulse duration usually ranges from tenths of a nanosecond to few nanoseconds. Designers are guided by the rule of achieving a wideband pulse spectrum that covers the desired frequency range while maximizing the radar energy potential. The latter is defined as the ratio of transmitter power to the receiver sensitivity. As a rule, the receiver sensitivity (usually of a stroboscopic receiver) is limited by about 100 μV without using special methods.

In order to increase the energy potential, designers increase the excitation pulse amplitude. Increasing the amplitude of the pulse with a duration of less than a nanosecond over a hundred volts are associated with technical difficulties, increasing the power consumption of the radar, and increasing the noise level. However, the use of Fourier transform theory makes it possible to increase the amplitude of the return signal of the target, not by increasing the amplitude of excitation pulse of the transmitting antenna, but by the method of optimizing the duration of this pulse.

4.4.2.1 Optimization of the transmitter pulse duration by the criterion of the radiation spectrum maximization at a given frequency

Experimental tests were performed to confirm the existence of optimal duration pulse for a chosen antenna with known central frequency. These research results were published in a scientific journal *Aristov, V. (2016) Optimization of the transmitter pulse duration by the criterion of the radiation spectrum maximization at a given frequency. Automatic Control and Computer Sciences. 50(4), 220-225. Springer Link*, see Appendix 4.4.

Experiments were conducted on the model of the radar used for both the subsurface sounding and as an active human motion sensor behind obstacles. In the experiment, a wideband (20 GHz) real-time oscilloscope was used as a receiver. A trapezoidal form pulse former with fixed pulse rise/fall times, but variable pulse width in the range from 0 to 1000 ps was used. The pulse former was assembled according to the classical scheme based on two step recovery diodes (SRD).The UWB antenna system consisted of two shielded Bow-Tie type antennas. A formula was obtained for calculating this duration for specific values of the frequency and rise times, as well as for the antenna excitation pulse decay. The results of this research confirmed that the level of the target return signal of the radar with a pulse excitation antenna can be raised not only by increasing the

radar receiver sensitivity or by increasing the antenna excitation pulse amplitude, but also by selecting the optimal duration of the excitation pulse duration.

4.4.3 Remote life-sign (cardiac and respiratory movement) detection system device prototype

A prototype device was presented at *Invention and Innovation Exhibition MINOX 2016*. The exhibition took place at the Riga Technical University, from 7th to 8th of October 2016. The exhibition was organized as the main event of Latvian Inventors Day with the aim of promoting inventiveness in the society, and fostering the commercialization of inventions. Poster presented in the exhibition is shown in Appendix 4.5.

The device is based on the impulse radar sensor that sends short, low energy electromagnetic pulses and receives the reflected pulses from the medium being monitored. By processing the reflected signal, it is possible to estimate both the environmental parameters and their changes. If any motion occurs within the operation area of the device e.g., cardiac, respiratory or other human movement, then the reflected signal varies and this can be detected by the highly sensitive receiver developed at the Institute of Electronics and Computer Science. Using original digital signal processing methods, it is possible to separate signals related to cardiac and respiratory movements.

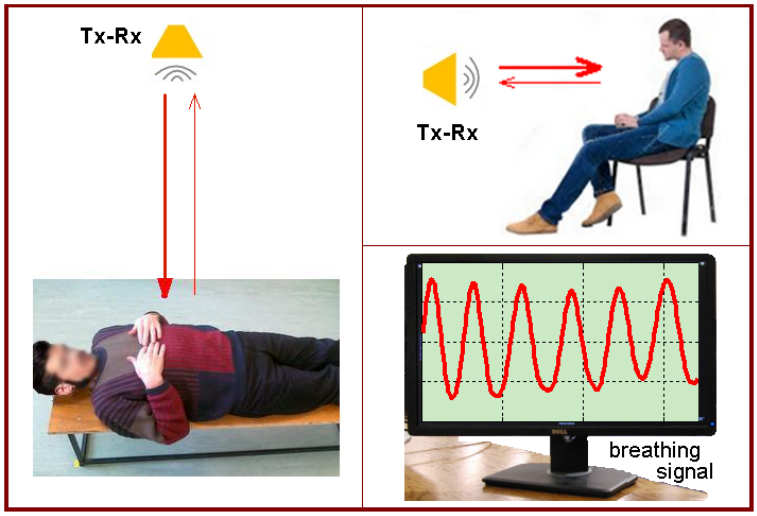

Figure 4.4.9: Remote life-sign detection system.

The device serves for the remote detection of human life-signs (breathing, heartbeat, movement). The life-signs can be detected behind walls and other non-metallic obstacles as well. The presented device can be used for:

- medical purposes, e.g., in hospitals to remotely monitor the patient's or infant's respiratory rate during sleep,

- security purposes, e.g., for detecting living persons or beings in the room or behind the wall,
- rescue operations, e.g., searching for people in the rubble that are showing signs of life,
- research work, e.g., for animal activity monitoring.

4.4.4 Undergraduate student assisted research

Two undergraduate students were involved (part-time) during this project period to assist the radar group in experimental research and carrying their own research work as a part of their bachelor thesis at the university.

4.4.4.1 Structure inspection using wall and ground probing radar

In this bachelor thesis, the application of impulse radar technology in testing concrete structures was studied. The goal of this bachelor thesis was to inspect a concrete structure and to measure the moisture level in a non-destructive manner. To achieve this goal, several tasks were defined: Analysis of impulse radar sensors, antenna tests, building bulkhead analysis and experimental signal processing.

To measure the moisture level of a construction, the dielectric permittivity has to be measured. In order to do that, the travel time of a signal in any given medium has to be measured and from this, the dielectric permittivity using Eq. 4.4.3 can be calculated .

$$\varepsilon = \left(\frac{c \cdot t}{2 \cdot x}\right)^2 \tag{4.4.3}$$

Where ε - dielectric permittivity, c – speed of light in vacuum, t – signal propogation time in medium, x – medium thickness.

The test setup consisted of a concrete wall, which thickness is 12.5 cm, where the radar was positioned 50cm from the wall (Fig. 4.4.10). For the test planar bow-tie antennas were used. A-scan data was acquired (Fig. 4.4.11a). Afterwards it was possible to achieve B-scan data throughout the length of the wall (Fig. 4.4.11b).

The concrete wall as an experimental object worked as planned. Knowing its thickness, we could calculate the travel time of the signal and then calculate the dielectric permittivity.

4.4.4.2 Room change and object movement detection sensor solutions

In this bachelor thesis, an overview of different room change and object movement detection sensors was prepared. Structure of the sensors, basic principles of operation and their properties were analysed. Sensors were compared with

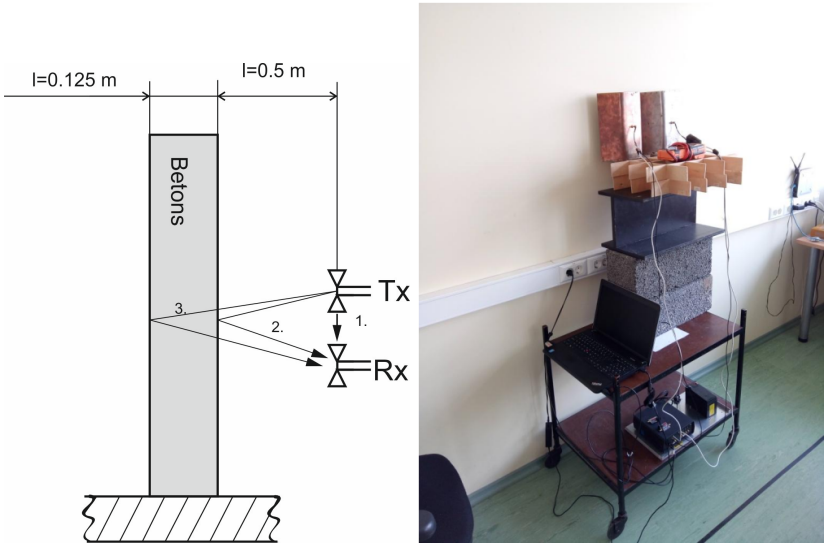

(a) Test setup (b) Experiment

Figure 4.4.10: Concrete wall test set up and experiment.

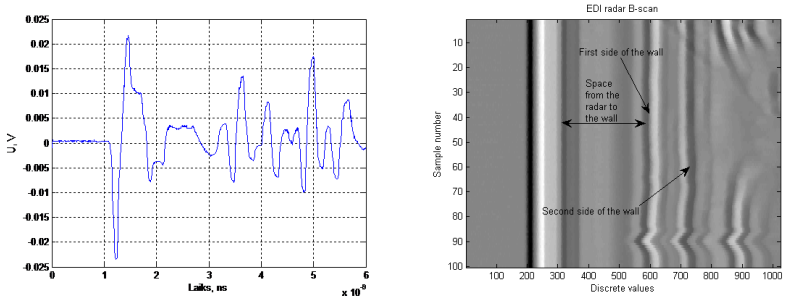

(a) A-scan (b) B-scan

Figure 4.4.11: Experimental EDI radar prototype.

each other. Calibration and distance measurements were performed with ultrasonic sensor and ultra-wide band radar to increase their measurement accuracy. Operation comparison was made measuring more than one object at a time. Doppler and passive infra-red sensors were compared.

Ultrasonic sensor calibration and distance measurements were made in an empty room with sensor lifted 1.2m off the ground and closest wall being 3m away. Two measurements at fixed distances were taken to calibrate ultrasonic sensor and, for the rest of the measurements, signal envelope was found using Hilbert transformation for easier signal analysis (Fig. 4.4.12).

UWB radar calibration was similar to ultrasonic sensor calibration but additional spacing between antennas needs to be taken into consideration (Fig. 4.4.13).

To understand advantages and disadvantages of the ultrasonic sensor and the

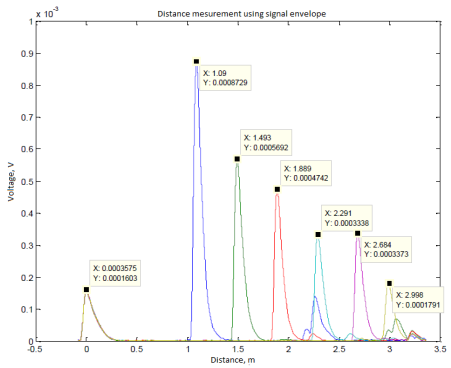

Figure 4.4.12: Distance measurement using signal envelope.

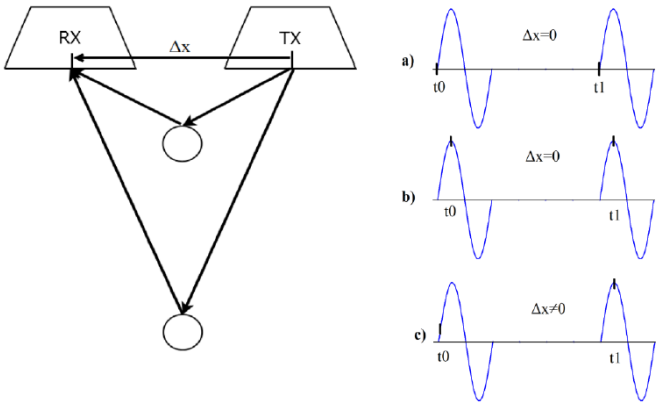

Figure 4.4.13: Radar sensor measurement scheme and reference point consideration

UWB radar, experiments with two objects were used. In the first experiment, one object was placed in front, and the other was placed behind so that it was partially visible (Fig. 4.4.14a). During another experiment, the second object was placed completely behind the first one (Fig. 4.4.14b).

In calibrated distance measurements taken with ultrasonic sensor, accuracy depends on used method. Using direct signal between transmitter and receiver as reference and reflected signal as an indicator of object location, the measurements were the most accurate, with distance error under 1% (Fig. 4.4.12).

For calibration of the UWB radar, the antenna positions were taken into consideration. After calibration, signal drift was observed (Fig. 4.4.15a). After eliminating signal deviation, measurement accuracy improved with error under 1.37% (Fig. 4.4.15b).

In the first case where one object was in front and second was behind but partially visible, both ultrasonic sensor and UWB radar measured their distances accurately. In the second case where the second object was completely behind the first one, only UWB radar detected the second object. Ultrasonic sensor measures distance more accurately from solid objects which reflect sound eas-

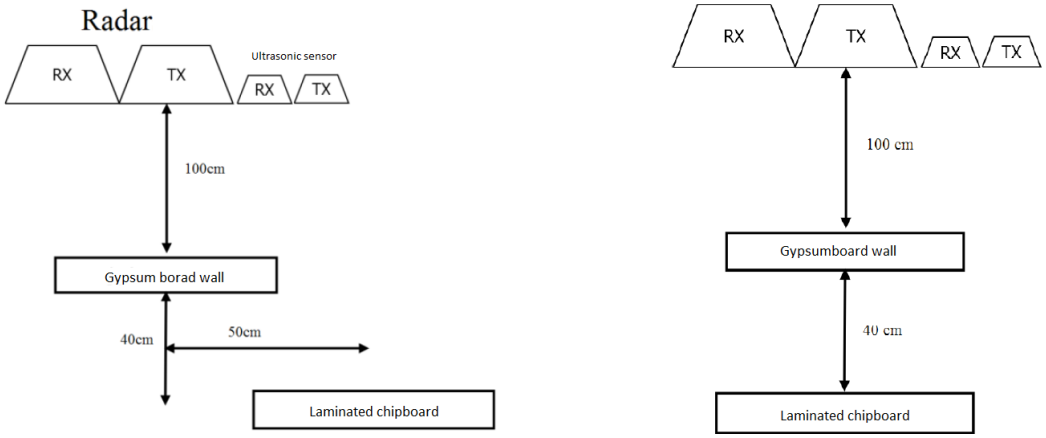

(a) (b)

Figure 4.4.14: Measurement schemes.

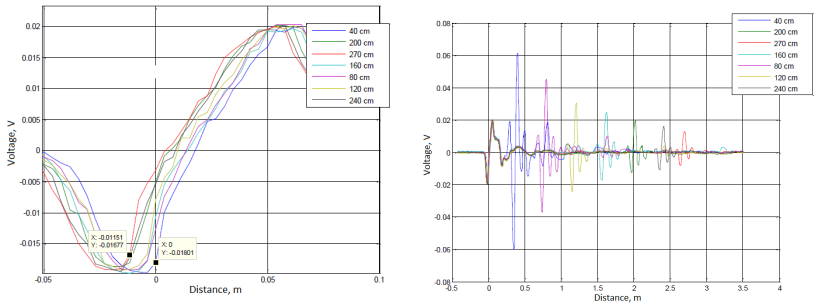

(a) Radar sensor time base drift (b) UUWB Radar sensor reflectogram

Figure 4.4.15: UWB Radar sensor distance measurements.

ily. As radio impulses penetrate objects, UWB sensor provides a possibility to observe objects which are directly visible.

4.4.5 Summary

The following results obtained within the reporting period 3 can be emphasized:

- UWB sensor signal processing methods were developed and experimentally tested for 2D tracking of moving objects. The multi-channel radar sensor prototype developed by the group was used in these experiments.
- Research on detection of small moving target (object) in ultra-wide band pulse radar sensors systems was carried out. The aim was to investigate methods of small object movement detection that are masked by large signal reflections from other objects in the area covered by the radar sensor.

Karhunen Loeve transform was used to filter out small object movements from the reflected radar sensor signals.

- Experimental tests were performed to confirm the existence of optimal duration and rise/fall time of the excitation pulse for a chosen trapezoidal antenna with known central frequency. These research results were published in a scientific journal.
- A remote life-sign (cardiac and respiratory movement) detection system device prototype was presented at the Invention and Innovation Exhibition MINOX 2016.
- On Radar group's supervision, two electrical engineering bachelor students carried out studies of radar sensor applications as part of their bachelor thesis work. Experimental concrete water content tests were carried out. Advantages and disadvantages of radar sensors technology compared to conventional security sensor solutions (10GHz Doppler radar sensor, passive infra-red sensor, ultrasonic sensor) were tested. The experimental radar sensor prototype developed by the RADAR group was used within the experiments.

4.4.6 Conclusions and future work

- The research results and experimental hardware prototypes designed by the RADAR group can be potentially used to make new and innovative products. For example, remote human presence and vital life-sign solution could be used in smart houses or medical facilities. A radar sensor network could be used to track human location and movement inside an apartment or house.
- The work on improvement of Radar sensor hardware parts will be continued.
- Specific UWB radar sensor technology demonstration devices prototypes will be developed:
  - miniaturized human presence and vital life-sign monitoring radar sensor device prototype;
  - moving object tracking radar sensor system prototype.

Chapter 4.5

RTU TI group: Development of fiber optics transmission technologies

During the third reporting period, activities of the "Development of fiber optics transmission technology" group were focused on the tasks related to optical transmission system element analysis that could be more appropriate for a smart city applications. From the previous research work it was found out that the Passive Optical Network – PON transmission technology enhanced by wavelength division multiplexing (WDM) is the most appropriate for a metro and access network level that corresponds to a city scale with high branching possibilities. During the third period the following tasks were addressed:

- multiwavelength light source implementation based on parametric amplification;
- development of the nonlinearity coefficient measurement method to find out the most suitable optical fibers for WDM-PON network;
- investigation on the minimum channel spacing in the WDM-PON system taking into account channel bitrate, laser parameters and overall spectral and energy efficiency.

In the WDM-based PON, five separate stages of the optical signal transmission could be set off: (i) generation of a carrier signal; (ii) multiplexing the optical signals; (iii) transmission of optical signals along a fiber-optical link (FOL); (iv) separation of optical signals according to the wavelengths (frequencies); (v) reception, demodulation and detecting of signals (see Fig. 4.5.1.). The first and the fifth stages are linked to the chosen format of optical signal modulation. The second and the fourth stages are connected with the method that is used for assignment of channel central frequencies. The third stage is associated with the mechanisms of linear and nonlinear distortions that affect transmission of modulated signals in the optical fiber. The assignment of central wavelengths (or frequencies) of the channels is based on two ITU-T recommendations: G.694.1

and G.694.2. The former recommendation describes the fixed and elastic DWDM gratings. In case of a fixed DWDM grating, the recommendation determines only and solely the central frequencies of channels at different channel spacing values, e. g., 200, 100, 50, 25 and 12.5 GHz, while in the elastic DWDM grating case this recommendation determines not only the channel central frequencies, but also the width of frequency slot. In this case for assignment of central frequency of the channels a 6.25 GHz step is used (see Eq. 4.5.1), whereas for determination of the width of frequency slot twice as large step is taken, i. e., 12.5 GHz (see Eq. 4.5.2).

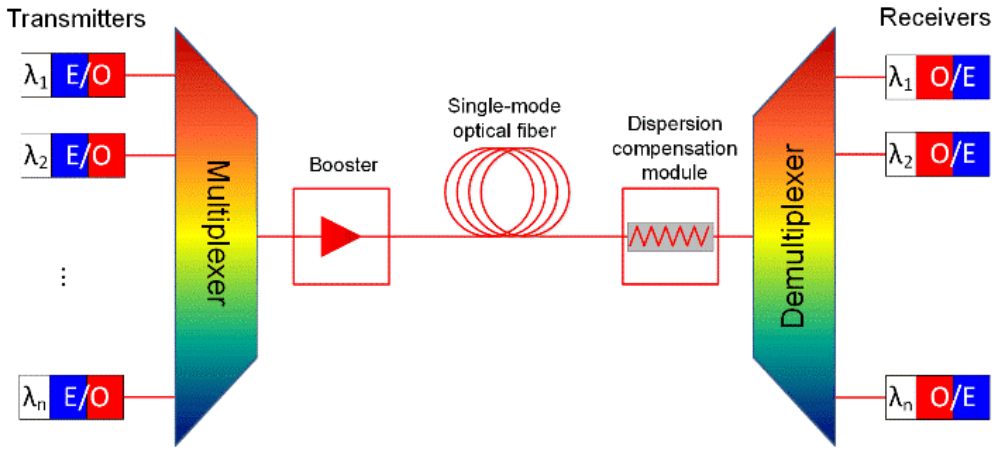

Figure 4.5.1: A simplified block-diagram of the WDM-based PON.

It has been necessary to introduce the elastic DWDM since the fixed DWDM grating works well, while in the WDM system all transmission channels operate at one data transmission rate and/or for modulation of optical signals the same modulation format is used. In the opposite case, either overlapping of optical channels occurs or the frequency resources of optical fiber are employed inefficiently.

$$f_c = 193.100 + n0.00625[THz], n = 0, \pm 1, \pm 2, \pm 3, ... \tag{4.5.1}$$

$$\Delta f_{width} = 12.5m[GHz], m = 1, 2, 3, ... \tag{4.5.2}$$

Analysis of the signal propagation along an optical fiber evidences that one of the main linear effects which significantly distort transmission of signals in the backbone optical networks is the ASE noise due to optical line amplifiers (OLAs), while the cross-phase modulation (XPM) is the main nonlinear optical effect. The level of ASE noise at the receiver's end directly depends on the noise factor of the EDFA used, on the gain itself determined by the distance between two OLAs, on the optical fiber attenuation coefficient and on the bandwidths of the electrical and optical filter used. This happens because the ASE noise after its reception and optical-to-electrical conversion appears as electrical noises. The XPM causes

just increase in the amplitude noises that arise due to dispersion observed in optical fibers. Such dispersion converts the phase modulation into the intensity modulation. Therefore, the XPM-related amplitude noises can seriously affect the intensity-manipulated signal (e. g., NRZ-OOK) transmission and the BER value at the receiver's end. It has been found that in case of 10 Gbps NRZ-OOK transmission with the quality of received signal being $Q = 7.3$, the level of XPM-related nonlinear noises exceeds noises by more than 20 times due to four-wave mixing (FWM). Considering the degrees of freedom for the optical signal — the amplitude (intensity), phase and state of polarization — the modulation formats that manipulate with the given degrees of freedom have been determined (see Fig. 4.5.2). The non-return-to-zero encoded on-off Keying (NRZ-OOK) is a historical solution for 10 G bit/s networks. The phase of the optical signal is already employed in the next stage of optical network development — namely, in the 40 G bit/s channel. In this case, one of the common modulation formats is the NRZ encoded differential phase-shift keying (NRZ-DPSK). The differential quadrature phase-shift keying (DQPSK) and the optical duobinary format (ODB) are an alternative solution for a data rate of 40 Gbps in a single wavelength.

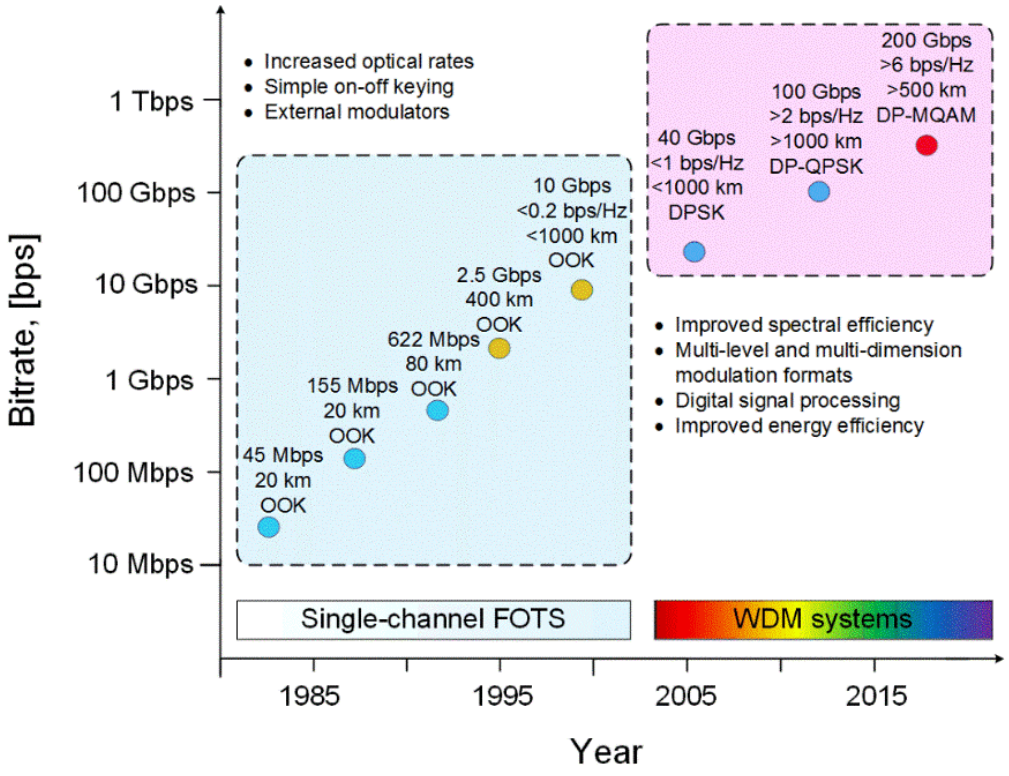

Figure 4.5.2: The development of transmission rate and modulation formats used in optical primary networks in the time period from 1980 to 2015.

As far as the optical signal state of polarization is concerned — even though this could also be applied to optical signal modulation (e. g., using the binary

orthogonal polarization state keying (2-POLSK)) — in the backbone optical networks of today this state is employed for additional optical signal polarization division multiplexing (PDM). For example, in case of 100 Gbps DP-QPSK solution two 50 Gbps QPSK signals are multiplexed after they have been in the particular state of polarization, one of them having linear X-polarization while the other — linear Y-polarization. The optical signal polarization division multiplexing (PDM or PolMux) allows reducing the width of frequency band required for transmission and the baud rate. For demodulation of such multi-level and multi-dimension modulation formats it is necessary to apply the coherent detection methods and digital signal processing (DSP). Dealing with coherent optical signal modulation formats one more distortion source should be taken into account — phase and frequency noises from the transmitter and receiver laser sources. This is especially important, since for cost minimization semi-conductor lasers are employed to generate radiation.

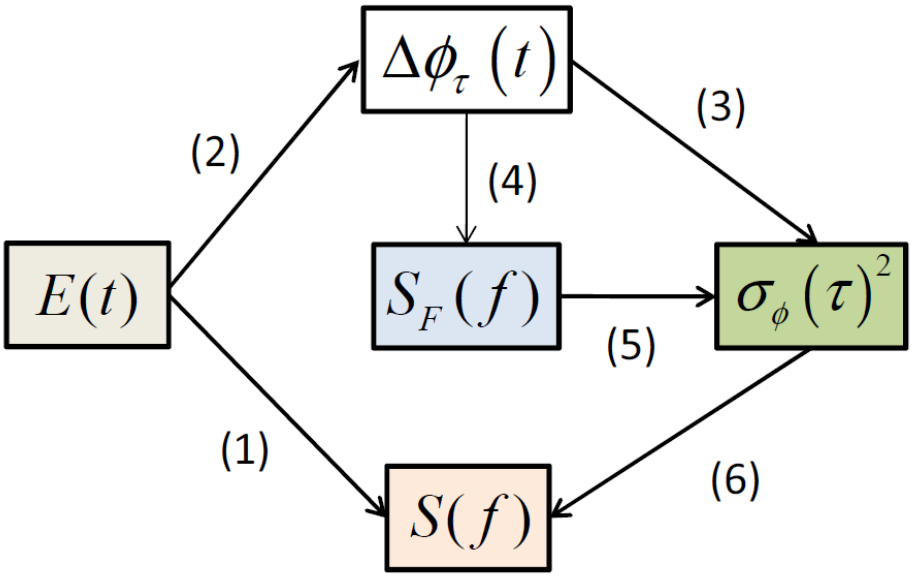

Figure 4.5.3: Relations among the complex amplitude $E(t)$ of laser field, the phase difference $\Delta\phi_\tau(t)$, the field spectrum $S(f)$, the frequency noise spectrum $S_F(f)$, the phase difference spectrum $S_{\Delta\phi_\tau}(f)$ and the phase noise variance $\sigma^2_\phi(\tau)$.

Several functions could be used for characterizing the laser field — the phase and frequency noise spectra are one of them. Fig. 4.5.3 shows the relations among the complex amplitude $E(t)$ of laser field, the phase difference $\Delta\phi_\tau(t)$, the field spectrum $S(f)$, the frequency noise spectrum $S_F(f)$, the phase difference spectrum $S_{\Delta\phi_\tau}(f)$ and the phase noise variance ${\sigma_\phi}^2(\tau)$. Mathematical expressions which are linking each of these parameters are given by eqs. (4.5.3) to (4.5.8).

$$S(f) = \langle \mid F[E(t)] \mid^2 \rangle \tag{4.5.3}$$

$$\Delta\phi_\tau(t) = \phi_n(t) - \phi_n(t-\tau) \tag{4.5.4}$$

$$\sigma_\phi{}^2(\tau) = \langle \Delta\phi_\tau(t)^2 \rangle \tag{4.5.5}$$

$$S_{\Delta\phi_\tau}(f) = 4\left(\frac{\sin(\pi \cdot f \cdot \tau)}{f}\right)^2 S_F(f) \tag{4.5.6}$$

$$\sigma_\phi{}^2(\tau) = 4\int_0^\infty \left(\frac{\sin(\pi \cdot f \cdot \tau)}{f}\right)^2 S_F(f)df \tag{4.5.7}$$

$$S(f) = F\left[\exp\left(-\frac{\sigma_\phi^2(\tau)}{2}\right)\right] \tag{4.5.8}$$

Note that the Fourier transformation is represented as $F[*]$ where $\langle * \rangle$ is the ensemble average.

Research on optical fiber nonlinearity coefficient measurements first of all involved development of the measurement method. It is based on the four wave mixing initiation in the fiber and requires two optical sources, namely pump and signal separated in the frequency domain that are passed through the fiber under test. Due to fiber nonlinearity there is a new frequency component called idler appearing at the output spectrum. Nonlinearity coefficient measurements are so called indirect, because the result is calculated from the measured input and output optical powers according to the created equation:

$$P_3(L) = \eta(\Delta\beta)(\gamma P_1(0) L_{eff})^2 P_2(0) e^{-\alpha L} \tag{4.5.9}$$

where P_1– pump power, P_2– signal power, $P3$– idler power, η– FWM efficiency, $\Delta\beta$– phase mismatch, γ– nonlinearity coefficient, L_{eff}– effective length, α– attenuation coefficient. From here, it can be seen that nonlinearity coefficient measurements also require other fibre's parameters. Therefore full fiber characterization is achieved that is necessary for the selection of the most appropriate fiber for data transmission over WDM-PON network. Experimental measurement method validation was performed on three different optical fibers: Corning SMF-28 ultra optical fiber, Draka enhanced single-mode optical fiber and highly nonlinear fiber. Obtained results have shown that measured values of the nonlinear coefficient are 0.78 $W^{-1}km^{-1}$ for SMF-28 fibers, 1.45 $W^{-1}km^{-1}$ for enhanced singlemode fiber and 10.68 $W^{-1}km^{-1}$ for highly nonlinear fiber that conforms to typical values. From all fibers under test the SMF-28 fiber fits the best for the WDM-PON network since it has the lowest nonlinearity coefficient.

Chapter 4.6

RTU WRL group: Development of the bacteriological quality monitoring system for city water supply system

Research goal: to develop a model of the quality control in a water supply system for protection against intentional or unintentional bacteriological contamination.

List of tasks in the period 3:

1. Experiments within pilot scale drinking water supply system by simulation of contamination events to evaluate the efficiency of drinking water on-line monitoring and early warning system
2. Development of algorithm for drinking water contamination event detection and alarm triggering
3. Long term drinking water quality monitoring at drinking water consumption point

4.6.1 Introduction

Drinking water safety has been a big issue for every civilization for centuries. During last decades, a huge step in development of measuring and computational technologies have been made, and it has opened a wide range of possibilities to provide safe and clean drinking water to every consumer of drinking water supply network. One of the aims of this project is to develop an early warning monitoring system for drinking water supply network, which should warn the water utilities in case of drinking water quality deterioration, thus helping to

prevent further distribution of contaminated water and reduce potential risks. In our project safety of DWDS should be achieved by development of monitoring and modelling tools, which could detect and recognize biological contamination in DWDS. Biological contamination was chosen as a primary risk, because most of the reported outbreaks are related to the sources of biological origin [14]. Biological contamination of various types and sources could enter DWDS, which reasons could be related to failure at the water treatment plant, pipe breakage/leakage, growth of bacteria, biofilm bacteria proliferation, and deliberate contamination.

Drinking water quality monitoring is a vital tool to ensure good drinking water quality. Although nowadays the legislation regulates drinking water monitoring procedure and frequency in most of the developed countries, normally it is not required to perform sampling in a drinking water distribution network more often than once per day. Apparently, in a worst-case scenario of the system failure this could lead to distribution of unnoticed contamination to customers. Moreover, rather high level of distrust of the drinking water quality exists within society, which asks for more reliable monitoring technologies. On-line drinking water quality monitoring systems could be a solution of these problems. Its ability to measure various water quality parameters with a time step of 1 minute allows to provide much more data, which should minimize the probability to overlook contamination, and therefore society could change the opinion on safety of drinking water.

In the framework of the project, a pilot scale on-line drinking water quality monitoring was carried out for more than 7 months and a total number of ¿ 3 500 000 readings was collected, which creates a new approach to analyse and understanding of DWDS. In this stage of the project the algorithms for detection and classification of different kind of contaminants were analysed and implemented in drinking water quality monitoring system. Five most commonly occurring types of contamination/deterioration were analysed and experimentally tested. Experiments were done in the previously made pilot scale drinking water supply network.

4.6.2 Experiments within pilot scale drinking water supply system by simulation of contamination events to evaluate the efficiency of drinking water on-line monitoring system

The purpose of drinking water quality monitoring and early warning system is to detect deliberate and accidental contamination. It is very important not only to detect the contamination but also classify the type of contaminant to determine the possible sources and causes of contamination and handle the situation correspondingly. Each kind of contamination might rise different risks to drinking water consumer and that leads to different action plans for each kind of contaminant.

In order to identify possible contamination events, the experiments were con-

ducted in previously constructed pilot scale drinking water supply system (described in project 1st and 2nd phase scientific report). The data were acquired with on-line drinking water quality monitoring system, and mathematical approach based on method of Mahalanobis distances and multidimensional spider graphs (cluster analysis) [15] was implemented to accomplish this task.

4.6.2.1 Simulation experiments of contamination events

To evaluate the capacity of on-line monitoring system to detect the possible drinking water contamination events, pilot scale experiments were done. Results of experiments are going to be published in Master's thesis and scientific publication on the next stage of project.
Although numerous chemical compounds are regulated for drinking water safety, legislative requirements for microbiological water quality are limited by only few indicator organisms, and total heterotrophic bacteria counts, which should be assessed by cultivation-based methods, which in turn have certain limitations. Moreover, biological contamination has higher impact on health in comparison with chemical water quality deterioration [16, 17, 18, 14], thus ideally biological contamination should be detected as soon as possible. Five contamination event scenarios in total were carried out (Fig.4.6.1), which aimed to detect the possible biological contamination events. Dilution of contaminant were assumed as 10% of drinking water flow in system. Temperature, pH, electrical conductivity (EC), chloride ions (Cl-), oxidation-reduction potential (ORP) and total organic carbon (TOC) were monitored in two measurement points with a time step of 1 minute to detect the possible contamination events. Also adenosine triphosphate (ATP) and flow cytometry measurements (FCM) of total and intact cell counts were conducted with a time step of 5 and 10 minutes (depending on the phase of experiment). Each contamination event was 15 minutes.

To achieve conditions that might be implemented in real scale situation, the hydraulic and physical parameters of drinking water supply system were following: flow – 0,21 m3/h, flow velocity – 0,1 m/s, pressure – 1 bar.

Experimental results showed that set of sensors installed in pilot scale drinking water supply system is able to detect the contamination (Fig.4.6.2) and example of measurement result from one sensor during the scenario with groundwater is shown in Fig.4.6.3. The latter shows EC changes at two sampling ports, located at 100 m from each other (equivalent with water retention time of 15 minutes). Detected changes of EC precisely corresponded to estimated time and duration of contamination with water retention time at monitoring points A and B respectively 16 and 32 minutes (theoretical and measured) and contamination event period of 15 minutes at both points.

One of the aims of the carried out experiments was to find and identify the possible correlations between physico-chemical and microbiological parameters. Experiments showed strong correlations between parameters. For example, correlations in the experiment with wastewater intrusion is shown in Fig.4.6.4, where Pearson correlation coefficient between TCC, ICC and EC is 0,85 – significant

Scenario indicator	Event description	Contaminant source	Volume
Untreated water	Simulation of failure in drinking water treatment plant and further distribution of untreated water	River Daugava (Kipsala, Riga)	6,15 l
Ground water	Simulation of pipe leakage and negative pressure in drinking water supply network which causes intrusion of ground water.	Ground water sample (ground water level lowering pump (Tvaika str., Riga)	6,15 l
Wastewater	Simulates the cross-connection between drinking water supply and wastewater collection systems.	Wastewater sample (wastewater pumping station (Daugavgrivas str., Riga) No	6,15 l
Deliberate contamination	Simulates the deliberate attack on drinking water supply system by injection of the microbiological pollution.	Artificial sample with *E.coli* pollution	6,15 l
Prolonged retention	Simulates the prolonged drinking water retention time in biologically unstable conditions with high possibility of bacterial regrowth	Sample from local (low usage) drinking water consumption point (RTU, Riga)	6,15 l

Figure 4.6.1: Description of experimental drinking water contamination events.

Scenario indicator	On-line monitoring					Analysis		Total
	TOC	pH	Cl	ORP	EVS	ATP	FC	
Prolonged retention (B)	0	1	1	1	1	1	1	6/7
Prolonged retention (A)	0	1	1	1	1	1	1	6/7
Untreated water (B)	1	1	0	1	0	1	1	5/7
Untreated water (A)	1	1	0	1	0	1	1	5/7
Ground water (B)	1	1	0	1	1	1	1	6/7
Ground water (A)	1	1	0	1	1	1	1	6/7
Wastewater (B)	1	0	0	1	1	1	1	5/7
Wastewater (A)	1	0	1	1	1	1	1	6/7
Deliberate contamination (B)	-	0	0	1	1	1	1	4/6
Deliberate contamination (A)	-	0	0	1	1	1	1	4/6

Figure 4.6.2: Evaluation of contaminant detection by the set of sensors (A – measurement station after 100 m, B – measurement station after 200 m, 1 – contamination is detected, 0 – contamination is not detected, - sensor out of service.

correlation.

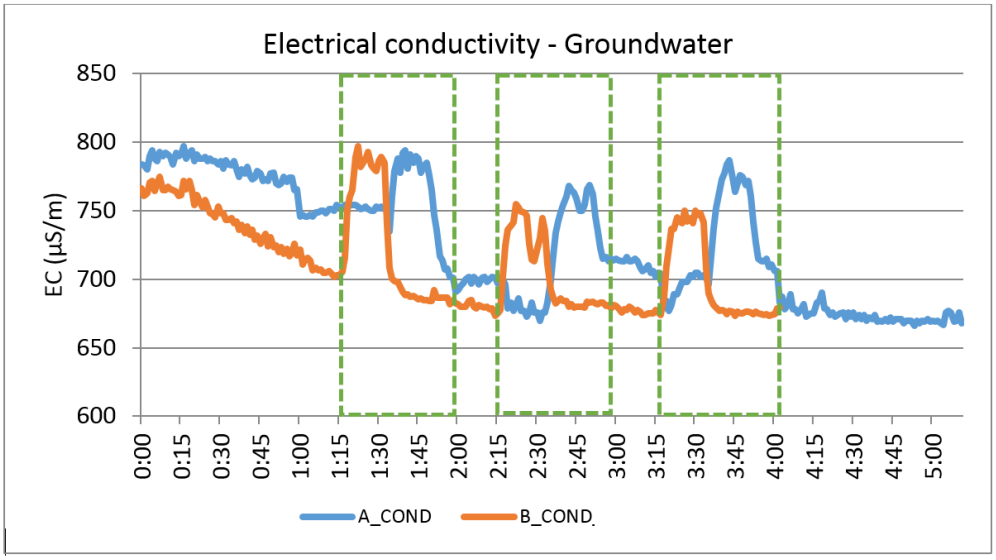

Figure 4.6.3: Changes of electrical conductivity over time during 3 contamination event repetitions. This example represents groundwater intrusion scenario, sensors – electrical conductivity, where A_COND – measurements after 100 m, B_COND – measurements after 200 m, dashed lines – contamination events.

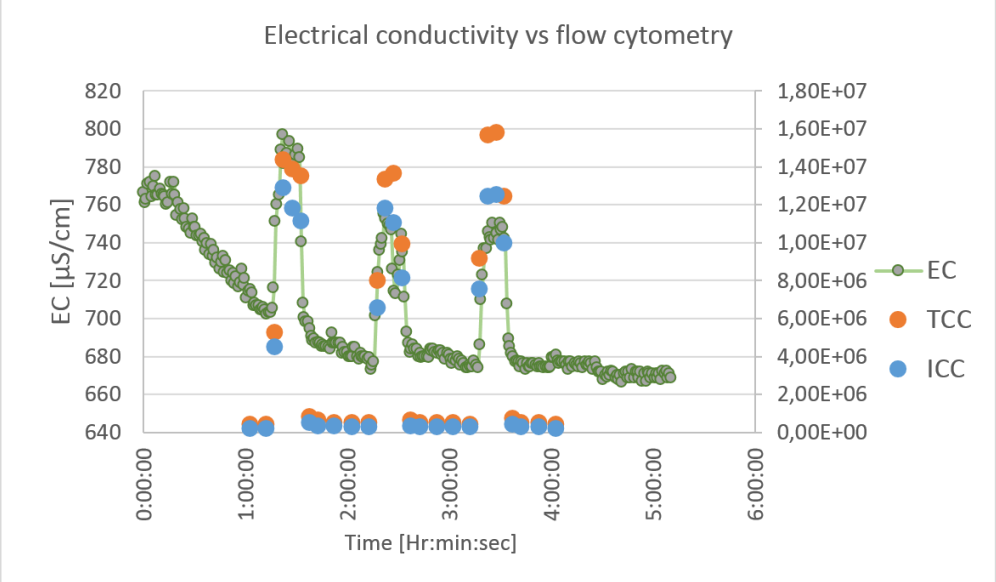

Figure 4.6.4: Changes of electrical conductivity and flow cytometry TCC and ICC during repeated (x3) wastewater contamination scenario.

4.6.2.2 Classification of the most possible drinking water supply system contaminants

Each of drinking water contaminants have different chemical and microbiological properties. Since there are more dangerous and less dangerous possible contamination agents for drinking water supply system, the classification of different contaminants by on-line drinking water quality monitoring system is vital for water utilities to develop suitable action plans for each type of contamination events.
Sensors responses, represented as clean (uncontaminated) and contaminated water ratio (wastewater and water with prolonged retention time), are shown as a multidimensional spider graphs on Fig.4.6.5. Figure shows that in a groundwater intrusion scenario, the graph leans to increased TOC ratio, though in a scenario of wastewater the peak is not so high and leans to EC. The figure demonstrates clearly different patterns of various contaminants. Cluster analysis approach was introduced to prove it with mathematical arguments and implement as an on-line tool for drinking water quality monitoring tool. Full report of experimental results will be compiled in scientific publication.

Literature studies showed that cluster analysis by implementation of Maha-

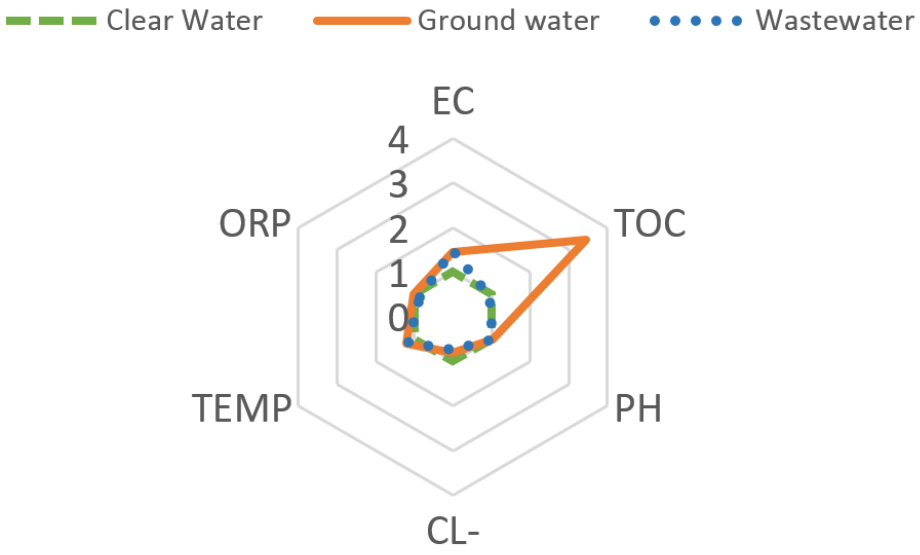

Figure 4.6.5: Example of sensor system response to contamination events.

lanobis distance is the most promising tool not only to make an early warning system alarm algorithm, which might be supported by algorithms consisting of Euclidian distance method [19], Pearson correlation Euclidean distance [20], canonical correlation analysis method [21], but also a contamination classification tool. It means that chosen algorithm solves two tasks simultaneously. Each measurement set was done in each time step forms as a data set, which might

be called as an object. In this approach, the term instance refers to the object in pre-defined class while example refers to the object to be classified. Both instances are multidimensional vectors [22]. In our case 6-dimensional vector analysis is done. A similarity measure is a real-valued function that quantifies the similarity between to object. The Mahalanobis distance is a unit-less value and a descriptive statistic that provides a relative measure of a data point's distance from common point, which can then be used to identify and gauge similarity of an unknown sample set to a known one [22, 15]. Principle used for calculation on Mahalanobis distance DM is if $p = (p_1, p_2, p_3, \ldots, p_n)$ and $q = (q_1, q_2, q_3, \ldots q_n)$ are two points in n-space, then the Mahalanobis distance between two points p and q is calculated:

$$D_M(p,q) = \sqrt{(p-q)^T S^{-1}(p-q)} \tag{4.6.1}$$

In which S is the covariance matrix of q. Contaminant classification is done by analysing the distance from it a classified point (class - c) in n-dimensional space:

$$D_{pcM}(p,c) = \sqrt{(p-\mu c)^T S^{-1}(p-\mu c)} \tag{4.6.2}$$

Where D_{pcM} is the distance from a point to a class and μc is the mean of all instances in class c. Assuming there are n types of contaminants, $c_1, c_2, \ldots, c_n$, each call contains many vectors. For any sample p to be identified, if

$$D_{pcM}(p,c_i) < D_{pcM}(p,c_j), j = 1,2,3,...,n; i \neq j \tag{4.6.3}$$

Because of the high variety of total values in reading the measured values must be extracted to make quantitative analysis of contaminants. The features made from raw results are – R (raw result), RB (Ration of raw reading and baseline), R_B (difference between raw reading and baseline), RRBx-y(ratio of RB for sensor x and RB for sensor y).
The Mahalanobis distances for different features of measurements are showed in Fig.4.6.6. Results shows that the best resolution between contaminants are gained by using the R_B feature where the threshold of each class is 5% of total Mahalanobis distance value.

Mahalanobis Distance	Untreated water	Wastewater	Ground water	Deliberate contamination	Prolonged retention
R	7,79	7,87	7,57	6,72	8,21
RB	7,72	7,82	8,21	8,16	7,67
R_B	9,11	5,31	4,48	9,43	8,12
RRBx-y	20,34	7,81	7,72	6,92	10,17

Figure 4.6.6: Mahalanobis distances for various contaminants.

Further analysis of algorithm performance has to be done to evaluate the false classifications of contaminants by using different dilution of contamination agents.

4.6.3 Development of algorithm for drinking water contamination event detection and alarm triggering

The algorithm of drinking water contamination event detection is based on contamination classification algorithm described in previous chapter. In the alarm triggering procedure the Mahalanobis distance in every time step is analysed and compared to it in a normal – base line situation. If the certain Mahalanobis distance for time step exceeds the threshold value for ratio between base line and measurements done in time step the alarm is triggered. If the distance leans to some previously set values for certain type of contaminant, corresponding alarm level is triggered, based on the threat and size of the risk to health of society.

4.6.4 Long term drinking water quality monitoring at drinking water consumption point

The existing legislation regulates that the drinking water quality monitoring should be done once a day at different points of distribution network. This approach to quality monitoring has a huge drawback that there are no daily or hourly quality changes analysed. This might be a crucial issue during the contamination events described in previous chapters. For better understanding of drinking water quality variations due to hydraulic conditions in distribution network, caused by temporal water consumption fluctuations, an intensive drinking water quality monitoring measurements were done. The measurements were done in pilot scale system located in laboratory of Riga Technical University Water Research Laboratory and in the real scale distribution network of Riga city.

4.6.4.1 Long term drinking water quality monitoring in a pilot scale drinking water supply system

The pilot scale system (Fig.4.6.7) is described in the report for project periods 1 and 2. Temperature, pH, electrical conductivity (EC), Cl ions (Cl-), oxidation-reduction potential (ORP) and total organic carbon (TOC) were measured in the system. Drinking water was monitored during 7 months with a time step of 1 minute. During the last months of studies a turbidity sensor was installed at the measurement station B. So far, the total amount of readings in studies is more than 3 500 000. However, the large amount of collected data led to an issue on data collection and analysing system. The system should be improved and implemented in Mathlab environment, which would allow to do on-line analysis of data and also improve the collection and saving of data. For example, less relevant data in normal case situations might be stored every 10-15 minutes, however, data from contamination or drinking water quality variation periods might be stored with a time step of 1 minute. This approach might reduce the stored data amount by 10-15 times.

Figure 4.6.7: Lab-scale (pilot scale) DWDS.

Fluctuations of drinking water parameters were observed during long-term monitoring. Changes in EC during 11 weeks is demonstrated in Fig.4.6.8, where data are plotted against calendar week. Although completely stable results were not expected, weeks 4, 5, 8 and 10 show more extreme variations than the rest. Hourly, daily or weekly variations were analysed, but no correlations have been found, and the cause of these variations is not evident. However, most likely it is related to hydraulic conditions in the network. For example, changing water consumption would lead to water stagnation in the distribution network, or vice versa – delivery of fresh water from the water treatment plant. Moreover, the studied DWDS is supplied from both treated surface water and groundwater, which have different initial parameters, thus changes in water consumption could lead to different incoming water, or distribution of water from water reservoirs, which are used in Riga DWDS for compensation of drinking water consumption fluctuations.

Due to ability of on-line monitoring system to observe different patterns of drinking water quality, a systematic change of water parameters was detected. An example of such a pattern for temperature measurements is demonstrated on Fig.4.6.9. Drop of temperature was observed every Monday, Wednesday and Friday morning during all monitoring period (11 weeks). Importantly, no correlations with internal or external air temperature were found, which indicates that it is not caused by warming/cooling due to external environment. The plausible explanation is regular changes of water consumption in a large industrial/public building nearby. In our case it could be related to a swimming pool

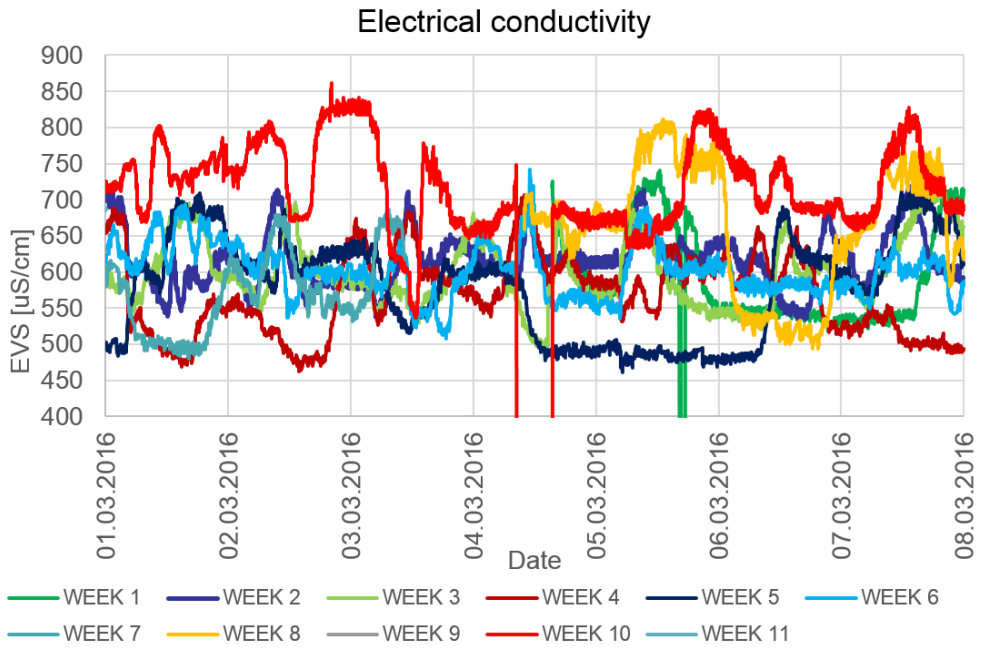

Figure 4.6.8: Fluctuation of electrical conductivity during long term monitoring.

situated near by the laboratory (about 100 m), where the water is recharged during the time of decrease of water temperature. Water recharge causes the increase of water flow/velocity, and supply with water with lower water retention time subsequently, which leads to lower water temperature at monitoring point.

This finding highlights the advantages and potential of continuous on-line monitoring. It is particularly important to understand systematic changes of drinking water parameters, and consider those, when defining a baseline for the early-warning system. Detection of new correlations and proofs of local hydraulic influences on drinking water quality what might lead to influence to decent area of DWSS.

Long term on-line drinking water quality monitoring provides a new possibility for water utilities to understand water quality variations and determine the health of DWSS. Results of the first steps in long term monitoring are summarized in article "Dejus, S., Rusenieks, R., Nescerecka, A., Nazarovs, S., Juhna, T., (2016) Long Term Drinking Water Quality Monitoring in Drinking Water Supply Systems by On-Line Sensors" (Appendix 4.6). Results were also presented in RTU 57th International Scientific Conference and IWA 8th Eastern European Young Water Professionals Conference. The demonstration of pilot scale drinking water supply system and on-line drinking water quality monitoring system to professionals of water sector was carried out during the RTU 57th International Scientific Conference ("Drinking Water Quality Monitoring and Safety of Drinking Water Supply Network"). The results of biological stability from previous period, obtained with different methods, was analysed, and the

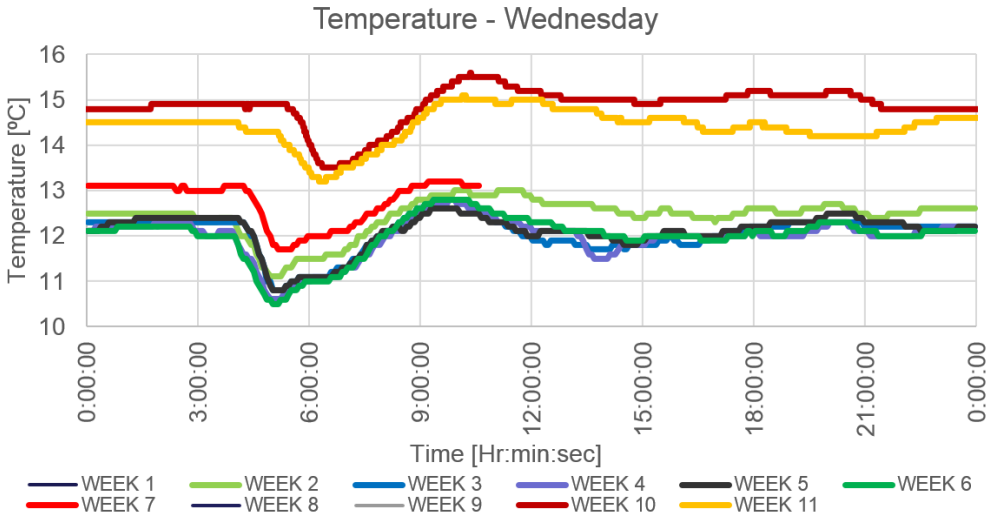

Figure 4.6.9: Diurnal fluctuations of temperature on Wednesdays during long term monitoring. Similar patterns were observed for Mondays and Fridays (not shown). Temperature was stable during other days of the week.

methods were compared (Fig.4.6.10). The results show that both methods could

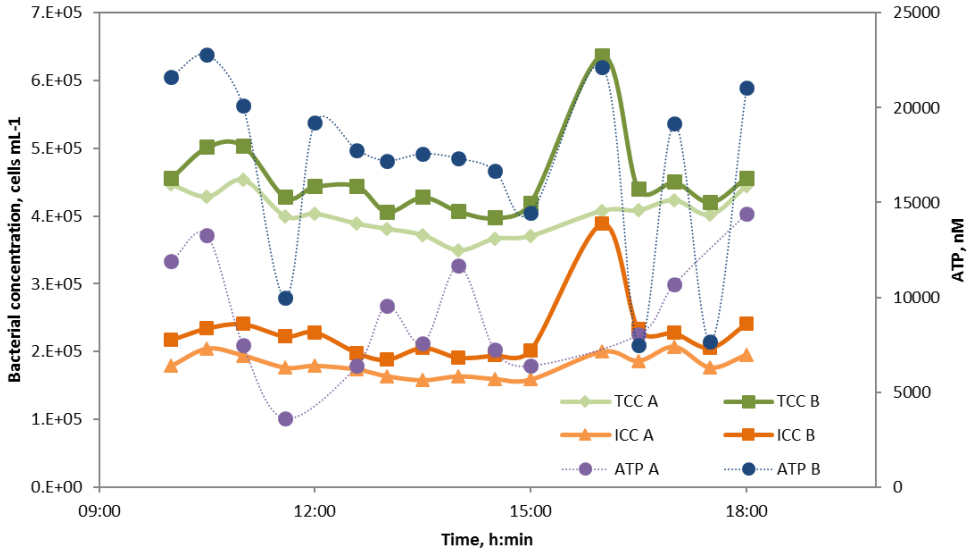

Figure 4.6.10: Changes in ATP, TCC and ICC during 8 h monitoring, and a response of these parameters to a change of the flow rate (16:00). A and B indexes correspond to the samples from the Stations A and B.

be used for microbiological quality characterization. These demonstrate clear difference between points A and B, where the latter has higher ATP, ICC, and

TCC values during all observation time, which could be explained by biofilm influence. This also could be a reason why changes in point A were not detected – increase of biomass is likely a function of distance, which is particularly interesting and important for a potential contamination/system failure localization. FCM ICC and TCC showed better response to changing flow rate, than ATP measurements. This could be explained by low sensitivity of the instrument for minor bacterial changes (drinking water bacteria normally have low ATP content), or it can be influenced by extracellular ATP. When compared with recently published research article, where extracellular ATP behavior was specifically investigated during water chlorination, the difference with this experiment was that this was a dynamic system and not static, as in the mentioned study [23]. The study of ATP was finalized and published in the research article "Nescerecka, A., Juhna, T., Hammes, F., 2016. "Behavior and stability of adenosine triphosphate (ATP) during chlorine disinfection" Water Res. 101, 490–497" (Appendix 4.7). In turn, flow cytometric ICC measurements were performed according to previously optimized protocol, which was published as a scientific publication "Alina Nescerecka, Frederik Hammes, Talis Juhna, "A pipeline for developing and testing staining protocols for flow cytometry, demonstrated with SYBR Green I and propidium iodide viability staining", Journal of Microbiological Methods" (Appendix 4.8).

4.6.4.2 Long term drinking water quality monitoring in a real scale drinking water supply system

Long-term monitoring with FCM ICC and TCC methods was performed in two locations in Riga drinking water distribution system. TCC and ICC were measured weekly during one year in order to understand seasonal effect on bacterial parameters. The samples were taken in drinking water tap, where water has different water retention time, and possibly water sources (Riga distribution system is supplied by treated surface water and groundwater, which sometimes could be mixed or change each other at the same location). One of the sampling location is in the same building as the pilot system. Though, the reason it was not performed in our experimental system was that it the experiment started before it was ready to use – it was started during previous stage of the project as reported before, and lasted for 1 year.

Clear seasonal variations in TCC and ICC were observed in the drinking water distribution network samples over 12-months (n = 48). One-year monitoring showed that TCC values of the DN sample that originated from treated surface water varied from 0.67 to 5.87 x 105 cells mL-1, with a mean value 2.75 +- 1.41 x 105 cells mL-1 (CV = 51 %) (n = 48) (Fig.4.6.11 a), and ICC values were from 0.1 – 3.75 x 105 cells mL-1, with a mean value 1.46 +- 0.95 x 105 cells mL-1 (CV = 65 %) (n = 48). Interestingly, generally higher bacterial concentrations were observed during warm time of the year: all ICC and TCC values, which were higher than the average, occurred in a time period from May to October, and were lower in the rest time of the year, following similar trend as a temperature

at the treatment plant. TCC and ICC values of the mixed sample were different from the surface water sample and showed less seasonal dependency. TCC was from 1.98 – 6.76 x 105 cells mL-1 (mean = 4.41 +- 1.36 x 105 cells mL-1 (CV = 31 %) (n = 48)) (Fig.4.6.11 b), and ICC values varied from 0.44 x 105 – 4.37 x 105 cells mL-1 (mean = 2.20 +- 1.05 x 105 cells mL-1 (CV = 48 %) (n = 48)), thus both TCC and ICC were significantly different from the first sample (P ¡ 0.05). Differences between warm and cold seasons were not as clear as in the example of surface water sample, however, clearly lower TCC and ICC were observed in a period from mid-January until April. Temperature in the tap was from 11.5 to 19.3 degrees C during all observation period, and relatively weak correlations between tap water temperature and TCC (R2 = 0.56) and ICC (R2 = 0.49) (Fig. 4.6.12) were obtained.

4.6.5 Conclusions and future work

The studies from the 3rd period of the project proved that the on-line drinking water quality monitoring systems have a huge potential and resource. Long-term experiments provided wide data range on drinking water quality parameters that have not been analyzed before in such an extent. Obtained results demonstrated high-resolution temporal variability, which will be interpreted and used for an early-warning system development. However, this large amount of data met technical issues in terms of data interpretation and analysis, which will be continued in the next project stage. Ideally, improvements in long term monitoring should be achieved by limiting the data storage and analysis amount, which would allow to adopt them for implementation in hydraulic and drinking water quality models. Moreover, those systems can be implemented as a tool in drinking water safety plan.

Successful approbation of the on-line monitoring system during simulation experiments demonstrated high sensitivity of the tool, which was corroborated with biological methods. Methods and algorithms, implemented for drinking water contamination event detection and identification, were tested and moved a step forward in development of early warning system. Future activities involve thorough work to continue modelling of various scenarios and development of algorithms. Improvements of algorithms could be done in amount of data to be stored to reduce the storage capacities. Also more experimental tests should be done to recognize the shortages of such systems, for example, a low concentration pollution of system and positive/negative alarm triggering events to evaluate the overall sensitivity of system. The topicality of issues addressed in this phase is very high in society and it is proved by publication in media (5 publications – radio, TV, web).

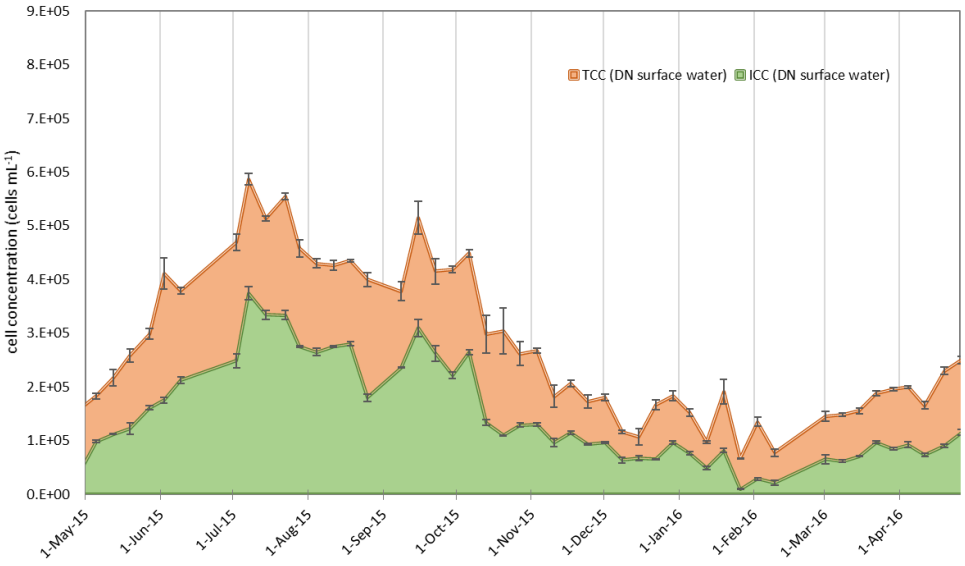

(a)

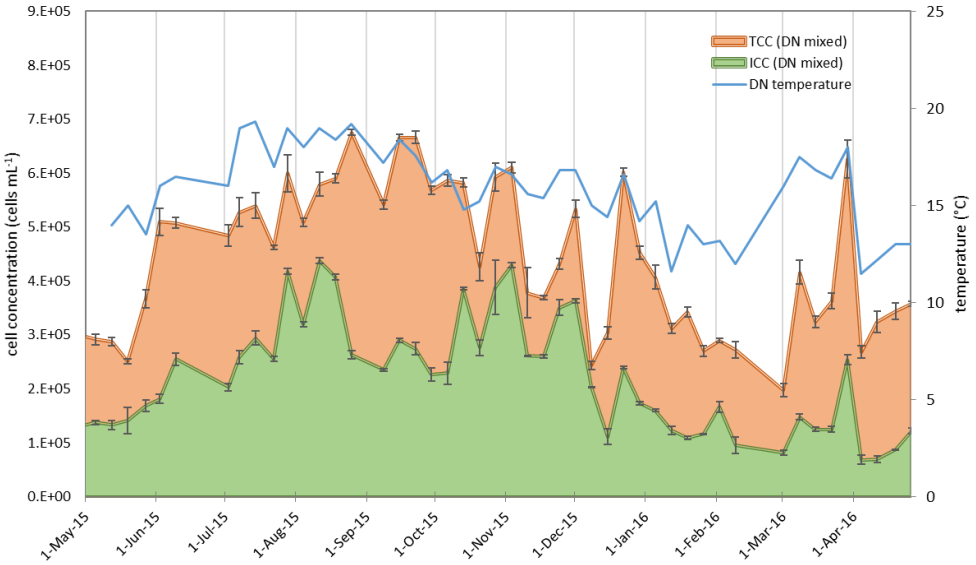

(b)

Figure 4.6.11: Temporal bacterial cell variations over long-term monitoring of the drinking water network (DN) sample, which was originated from treated surface water (a) and surface water, which could be potentially "mixed" with groundwater (b) (n = 48). (b) sample was taken in the university campus building, and temperature was measured as well.

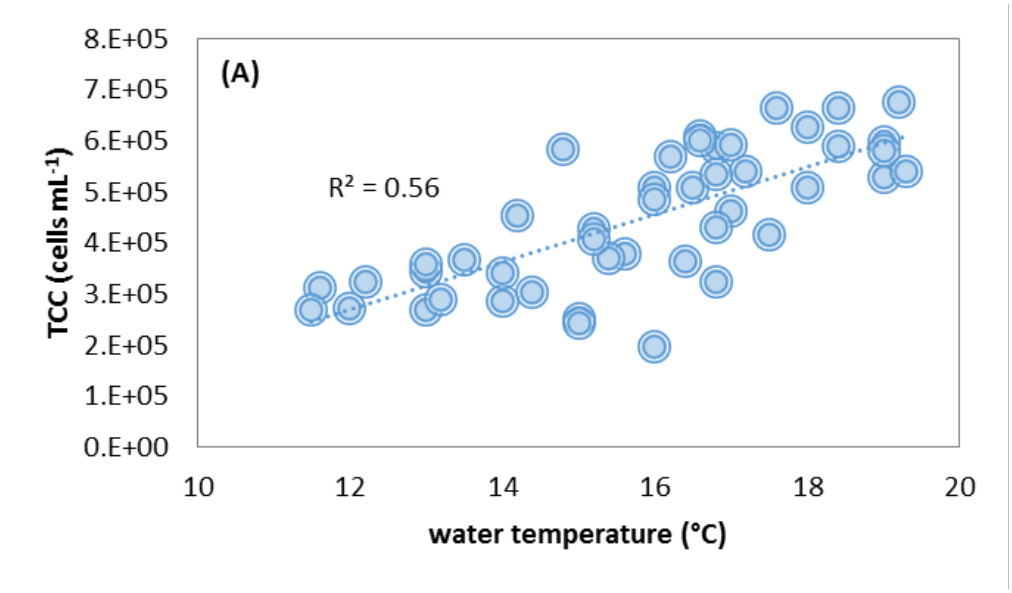

(a)

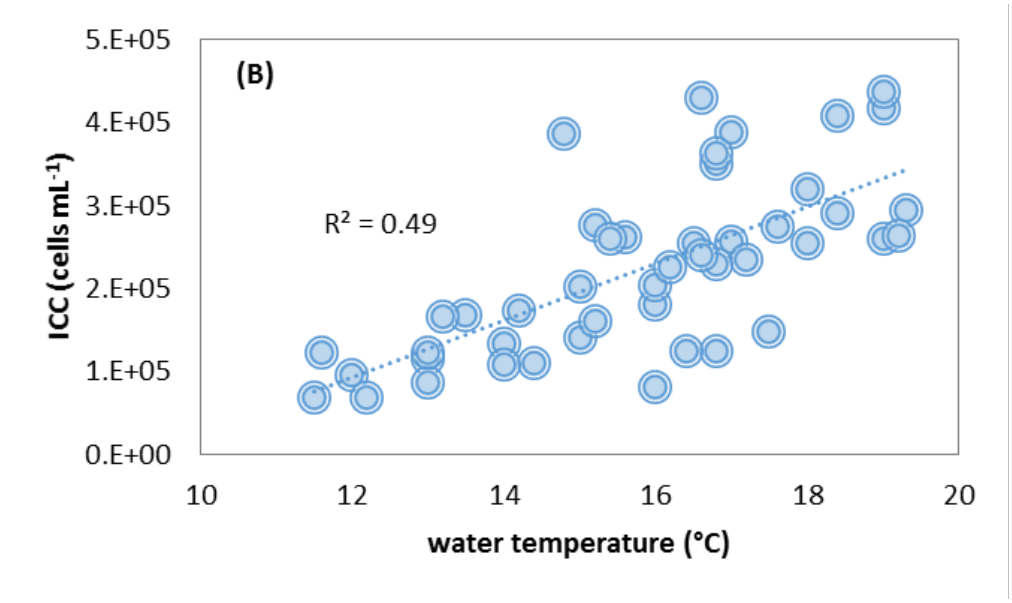

(b)

Figure 4.6.12: Correlations between DN water temperature and total cell count (a) and intact cell count (b) (n = 46).

Bibliography

[1] James Philbin Florian Schroff, Dmitry Kalenichenko. FaceNet: A unified embedding for face recognition and clustering. In *arXiv:1503.03832*, 2015.

[2] Andrew Zisserman Omkar M.Parkhi, Andrea Vedaldi. Deep face recognition. In *British Machine Vision Conference*, 2015.

[3] Yaniv Taigman, Ming Yang, Marc'Aurelio Ranzato, and Lior Wolf. Deepface: Closing the gap to human-level performance in face verification. In *Proceedings of the IEEE Conference on Computer Vision and Pattern Recognition*, pages 1701–1708, 2014.

[4] Color Feret. Facial image database. *Image Group, Information Access Division, ITL, National Institute of Standards and Technology (October 2003)*, 2003.

[5] Martín Abadi, Ashish Agarwal, Paul Barham, Eugene Brevdo, Zhifeng Chen, Craig Citro, Greg S. Corrado, Andy Davis, Jeffrey Dean, Matthieu Devin, Sanjay Ghemawat, Ian Goodfellow, Andrew Harp, Geoffrey Irving, Michael Isard, Yangqing Jia, Rafal Jozefowicz, Lukasz Kaiser, Manjunath Kudlur, Josh Levenberg, Dan Mané, Rajat Monga, Sherry Moore, Derek Murray, Chris Olah, Mike Schuster, Jonathon Shlens, Benoit Steiner, Ilya Sutskever, Kunal Talwar, Paul Tucker, Vincent Vanhoucke, Vijay Vasudevan, Fernanda Viégas, Oriol Vinyals, Pete Warden, Martin Wattenberg, Martin Wicke, Yuan Yu, and Xiaoqiang Zheng. TensorFlow: Large-scale machine learning on heterogeneous systems, 2015. Software available from tensorflow.org.

[6] Alex Krizhevsky, Ilya Sutskever, and Geoffrey E Hinton. Imagenet classification with deep convolutional neural networks. In *Advances in neural information processing systems*, pages 1097–1105, 2012.

[7] Yandong Guo, Lei Zhang, Yuxiao Hu, Xiaodong He, and Jianfeng Gao. MS-Celeb-1M: A dataset and benchmark for large-scale face recognition. In *arXiv:1607.08221*, 2016.

[8] Imagenet. Available at http://www.image-net.org/challenges/LSVRC/2014/.

[9] Ranjay Krishna, Yuke Zhu, Oliver Groth, Justin Johnson, Kenji Hata, Joshua Kravitz, Stephanie Chen, Yannis Kalantidis, Li-Jia Li, David A Shamma, et al. Visual genome: Connecting language and vision using crowdsourced dense image annotations. *arXiv preprint arXiv:1602.07332*, 2016.

[10] Adam Lerer, Sam Gross, and Rob Fergus. Learning physical intuition of block towers by example. *arXiv preprint arXiv:1603.01312*, 2016.

[11] Wenbin Li, Seyedmajid Azimi, Aleš Leonardis, and Mario Fritz. To fall or not to fall: A visual approach to physical stability prediction. *arXiv preprint arXiv:1604.00066*, 2016.

[12] Adrien Gaidon, Qiao Wang, Yohann Cabon, and Eleonora Vig. Virtual worlds as proxy for multi-object tracking analysis. *arXiv preprint arXiv:1605.06457*, 2016.

[13] Ray D Jackson and Alfredo R Huete. Interpreting vegetation indices. *Preventive Veterinary Medicine*, 11(3):185–200, 1991.

[14] WHO. Water safety in distribution systems. 2014.

[15] Prasanta Chandra Mahalanobis. On the generalized distance in statistics. *Proceedings of the National Institute of Sciences (Calcutta)*, 2:49–55, 1936.

[16] Cara Gleeson and Nick Gray. *The coliform index and waterborne disease: problems of microbial drinking water assessment*. CRC Press, 2002.

[17] National Research Council (US). Committee on Public Water Supply Distribution Systems: Assessing and Reducing Risks. *Drinking Water Distribution Systems: Assessing and Reducing Risks*. National Academies Press, 2006.

[18] Mark D Sobsey. Drinking water and health research: a look to the future in the united states and globally. *Journal of water and health*, 4(S1):17–21, 2006.

[19] Shuming Liu, Kate Smith, and Han Che. A multivariate based event detection method and performance comparison with two baseline methods. *Water research*, 80:109–118, 2015.

[20] Shuming Liu, Han Che, Kate Smith, Musuizi Lei, and Ruonan Li. Performance evaluation for three pollution detection methods using data from a real contamination accident. *Journal of environmental management*, 161:385–391, 2015.

[21] Shuming Liu, Ruonan Li, Kate Smith, and Han Che. Why conventional detection methods fail in identifying the existence of contamination events. *Water research*, 93:222–229, 2016.

[22] Shuming Liu, Han Che, Kate Smith, and Tian Chang. A real time method of contaminant classification using conventional water quality sensors. *Journal of environmental management*, 154:13–21, 2015.

[23] Alina Nescerecka, Talis Juhna, and Frederik Hammes. Behavior and stability of adenosine triphosphate (atp) during chlorine disinfection. *Water Research*, 2016.

Appendix 4.1
Pielikums 4.1

Selection of Informative Bands for Classification of Hyperspectral Images Based on Entropy

Appendix 4.2
Pielikums 4.2

Informative hyperspectral band subset selection based on entropy

Appendix 4.3
Pielikums 4.3

Karhunen-Loeve transform as a tool to eliminate signal's redundancy, when small targets detection

Appendix 4.4
Pielikums 4.4

Optimization of the Transmitter Pulse Duration by the Criterion of the Radiation Spectrum Maximization at a Given Frequency

Appendix 4.5
Pielikums 4.5

Remote Life-sign Detection: movement, breathing, hearbeat

MINOX 2016 poster

Appendix 4.6
Pielikums 4.6

Long term drinking water quality monitoring in drinking water supply systems by on-line sensors

Appendix 4.7
Pielikums 4.7

Behavior and stability of adenosine triphosphate (ATP) during chlorine disinfection

Appendix 4.8
Pielikums 4.8

A pipeline for developing and testing staining protocols for flow cytometry